UNIVERSITY OF CALIFORNIA,
IRVINE

Two-phase Flow Dynamics in Two Parallel Thin Micro-channels

DISSERTATION

submitted in partial satisfaction of the requirements
for the degree of

DOCTOR OF PHILOSOPHY

in Mechanical and Aerospace Engineering

by

Jingtian Wu

Dissertation Committee:
Professor Yun Wang, Chair
Professor Derek Dunn-Rankin
Professor Jack Brouwer

2020

DEDICATION

To

my parents and friends

in recognition of their

selfless support and unconditional love

Table of Contents

LIST OF FIGURES

LIST OF TABLES

ACKNOWLEDGEMENTS

I have acquired a lot of support financially and intellectually from faculty members, staffs and students during my six-year graduate career in Mechanical and Aerospace Engineering department at UC, Irvine. Equipped with those generous support, I am able to achieve every single academic milestone. I will never accomplish my research work and PhD study without their selfless help.

First, I would like to thank my PhD advisor, Dr. Yun Wang who brings me to the field of research on two-phase flow dynamics and provides me with great academic guidance, countless hours of time, full of encouragement especially when I encounter difficulties in my research work and life.

I am also indebted to Dr. Derek Dunn-Rankin, Dr. Jack Brouwer, Dr. Abraham Lee and Dr. Wenlong Jin for their service on my doctoral committee and thankful for their advice, suggestions and reviews on my thesis. They are unforgettable part of my study in UC, Irvine.

Finally, I would like to thank my parents in China who give me unconditional love, continuous encouragement and support so that I can move forward firmly towards my life goals. My debt to them is beyond any measurement.

CURRICULUM VITAE

Jingtian Wu

2013	B.E. in Mechanical Engineering, Shenyang University of Technology, China
2015	M.S. in Mechanical & Aerospace Engineering, University of California, Irvine
2020	Ph.D. in Mechanical & Aerospace Engineering, University of California, Irvine

ABSTRACT OF THE DISSERTATION

Two-phase Flow Dynamics in Two Parallel Thin Micro-channels

By

Jingtian Wu

Doctor of Philosophy in Mechanical and Aerospace Engineering

University of California, Irvine, 2020

Professor Yun Wang, Chair

Two-phase flow in micro-channels plays a critical role in micro-electro-mechanical systems, electronic cooling, chemical process engineering, medical and genetic engineering, bioengineering and etc. In PEM fuel cells, liquid water from humidified gas streams and electro-chemical reactions triggers two-phase flow in gas flow channels, which is one of the main reasons that reduce fuel cell performance and durability. The main goal of this thesis is to investigate two-phase flow dynamics in micro-channels at various superficial gas and liquid velocities and flow mal-distribution among multiple channels.

First, two phase flow in a single thin micro-channel is investigated to study the ranges of two-phase flow in the film flow regime, water fraction, and pressure drop using the Volume of Fluid (VOF) method which tracks the air-water interface in computation. The channel dimension is 164 mm by 3 mm by 0.3 mm. The numerical results are compared with experimental data, theoretical solutions and modeling data in terms of flow patterns, water fraction and pressure drop. The prediction indicates a film flow in the range of operation ($1.69\ m/s < u_g < 5.08$ m/s and $5 \times 10^{-5}\ m/s < u_L < 10^{-2}$ m/s), as observed experimentally, for the wall contact angle ranging

from 5° to 40° including varying contact angles at different walls of a channel. The contact angle is found to have a small impact on the gas pressure drop in the range of operational conditions as long as the two-phase flow pattern remains in the stratified flow regime. However, the contact angle influences the meniscus of the two-phase interface, which affects the optical detection of liquid thickness in experiment.

Two-phase flow dynamics in parallel channels is then experimentally studied due to its significance in many engineering applications. A system of two parallel thin micro-channels with shared inlet and outlet manifolds is designed for this study with one channel subject to single phase flow and the other to two-phase one. The channel dimensions are the same as those in the VOF study with similar operating conditions including the superficial gas and liquid velocities, which are $0.86\ m/s < u_g < 3.44$ m/s and $10^{-4}\ m/s < u_L < 10^{-2}\ m/s$, respectively. Film flow patterns are observed for all the cases of the two-channel study. The $\frac{Q_2}{Q_1}$ ratio of the two-phase (Q_2) to single-phase channel (Q_1) flow rate is defined as a direct measure to flow maldistribution. Derivation is performed, showing that the $\frac{Q_2}{Q_1}$ ratio is inverse of the two-phase flow amplifier ϕ or $\frac{Q_2}{Q_1} = \frac{1}{\phi}$. Three liquid water flow rates are examined in experiment, which represent three typical trends: 1.) For the highest water superficial velocity in the two-phase flow channel, i.e. 10^{-2} m/s, the ratio is found to increase with the overall air flow rate. The $\frac{Q_2}{Q_1}$ ratio reaches as low as about 0.2 at 0.86 m/s overall superficial gas velocity, and approaches to 0.65 at 3.44 m/s. In another words, the gas flow rate in the single-phase channel can be 5 times as large as that in the two-phase channel at 0.86 m/s overall superficial gas velocity though their dimensions are identical, showing the significant impact of liquid water on the gas flow rate. 2.) For the lowest water velocity, i.e. 10^{-4} m/s, the ratio shows a decrease trend, followed by an increase, as the average gas flow velocity

increases from 0.86 m/s to 3.44 m/s. It reaches as high as about 0.76 at 0.86 m/s overall superficial gas velocity, and drops to as low as about 0.55 at 1.72 m/s. 3.) For the intermediate water velocity, i.e. 10^{-3} m/s, two steady states are identified at 0.86 m/s overall superficial gas velocity with one having a ratio as high as about 0.69 and the other about 0.52. The rest follows the same trend as the case of liquid velocity at 10^{-4} m/s. The presence of the transition region at the two low liquid velocities may be due to the complex behaviors of the two-phase flow near the micro-channel exit.

Chapter 1

Introduction

1.1 Background and Motivation

Polymer electrolyte membrane (PEM) fuel cells, which convert the chemical energy stored in hydrogen fuel directly and efficiently to electrical energy with water as the only byproduct, have the potential to reduce our energy use, pollutant emissions, and dependence on fossil fuels [1, 43, 44, 90, 95, 96, 99, 105].A PEM fuel cell consists of bipolar plates, reactant gas channels, gas diffusion layers, and a proton-conductive membrane with platinum catalyst coated on both sides, called the membrane electrode assembly (MEA), as shown in Fig. 1 [2, 90, 95].

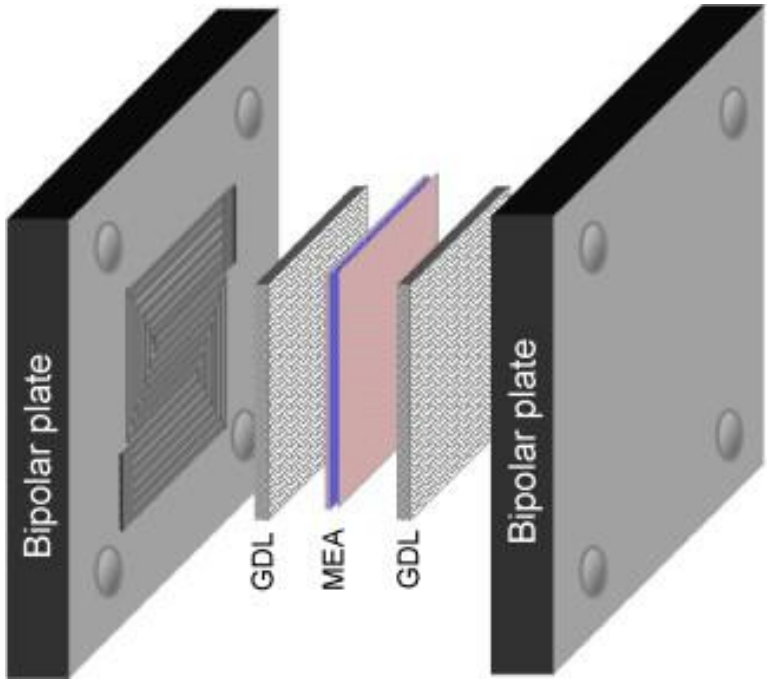

Figure 1: Schematic of a single PEM fuel cell [2]. The micro-channels are grooved in the bipolar plates to supply gaseous reactants.

Hydrogen fuel is injected into the anode gas channel, and diffuses to the anode catalyst layer on the membrane to produce electrons and protons via the hydrogen oxidation reaction (HOR). Protons carrying water molecules through the electro-osmotic drag are transported across the membrane to the cathode catalyst layer where they combine with oxygen and electrons to produce water as the only byproduct. Electrons are conducted via the external circuit to produce electricity.

Although PEM fuel cell possesses the characteristics of high power density, high energy efficiency, quietness and almost zero emissions, several technical challenges pose a barrier to its world-wide commercialization. One major challenge is the effective water management because the electrolyte membrane needs to be hydrated to conduct protons, while excess water causes flooding and thus prevents the reactant gas from reaching reaction sites. Effective water management is one of the key strategies to improve low temperature PEM fuel cell performance and durability [44, 95, 3]. Thus, understanding two-phase flow dynamics in micro-channels under PEM fuel cell operational conditions plays an important role in fuel cell design and water management.

1.2 Literature Review on Two-phase Flow in Micro-channels and Multi-parallel Channels

Two-phase flow in micro-channels has recently attracted people's concerns because of its wide application to modern and advanced science and technologies such as micro-electro-mechanical systems, electronic cooling, chemical process engineering, medical and genetic engineering, bioengineering and etc. [4]. Two phase flow in the channel can exhibit a variety of flow patterns at different superficial air and gas velocities. Experiments show that common flow regimes in large channels can be found in micro-channels as well. The commonly observed two-phase flow patterns of a gas and a Newtonian liquid in a large horizontal channel are depicted in Fig. 2 [5].

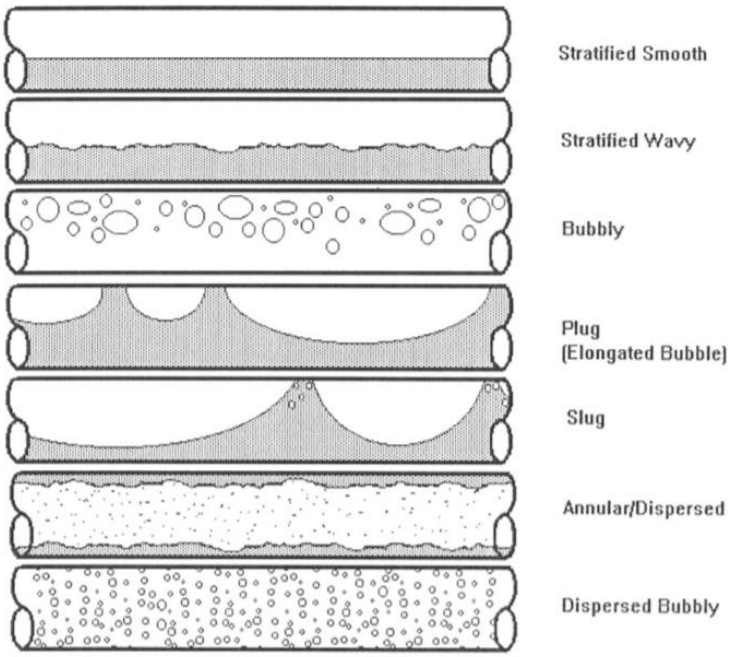

Figure 2: Major flow patterns in a large horizontal pipe [5].

In PEM fuel cells, water presence could be observed by the visualization techniques, such as optical methods [107] and X-ray [108] and neutron radiography [109], and is very different from traditional two-phase flow in other applications. One of the differences is that water content is introduced into the channel through the gas diffusion layer (GDL) after the oxygen reduction reaction (ORR) at the catalyst surface [90, 95, 96, 110, 112, 99, 114]. Water is also transported to the cathode from the anode through the electroosmotic drag when protons pass through the electrolyte. In addition, heat pipe effect was identified as a major mechanism for water transport via the vapor-phase diffusion in GDLs [115, 116, 118]. When water product forms a concentration gradient between the cathode and anode, water will diffuse back to the anode [119], including the anode flow channel. Flooding in the channel may lead to a partial or complete blockage of the channel for gas flow, thereby starving the reaction sites fed by the channel [6]. Thus, effective water management is critical to efficient operation of PEM fuel cells.

In order to resolve the water flooding problem, the two-phase flow patterns occurring in PEM fuel cells need to be investigated. Tüber et al. [107] designed a transparent fuel cell to study water buildup in the cathode and explain the phenomena of water flooding. They indicated that liquid water may clog the gas flow channel. Hussaini and Wang [7] presented images corresponding to the most common flow patterns in operational PEM fuel cells. These include single phase flow, droplet flow, film flow and slug flow as shown in Fig. 3.

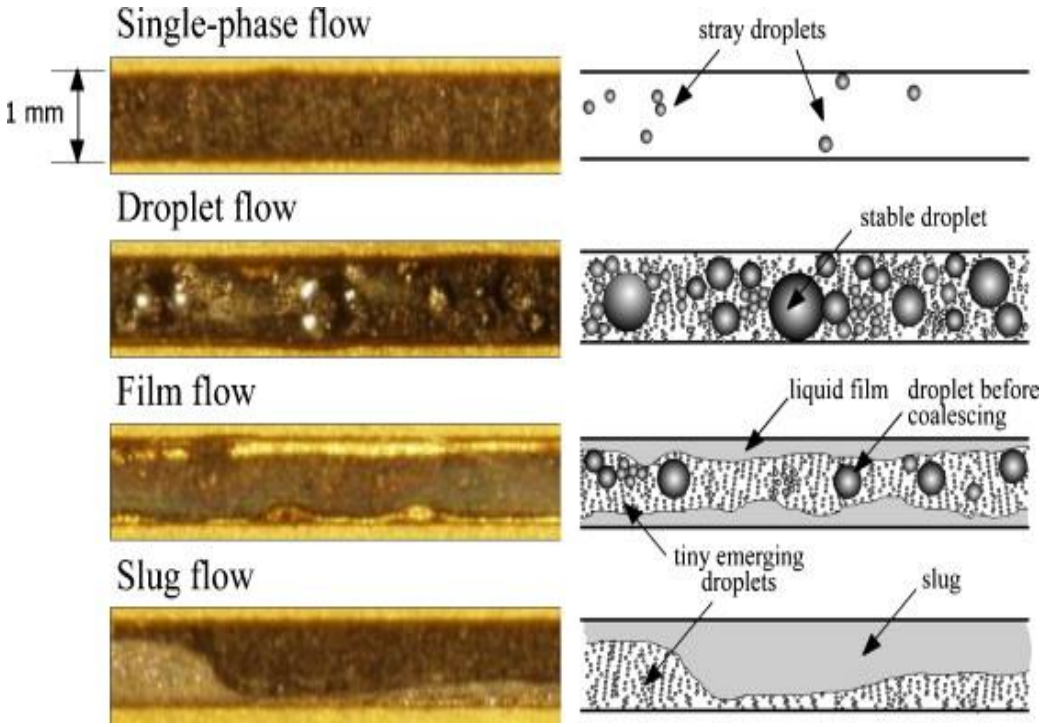

Figure 3: Common flow patterns in operational PEM fuel cells [7].

Ideally, water is expected to emerge uniformly under a uniform distribution of current density. In reality, flow maldistribution can cause uneven distributions of reactants among channels. Fig. 4 shows the two-phase flow and flow maldistribution in PEM fuel cell channels: both small and large droplets will hamper gas flow in the channels, and liquid water may clog a channel shutting

down the reactant supply [8]. Flow maldistribution is an important factor in reducing the fuel cell lifetime due to reactant starvation [9,10].

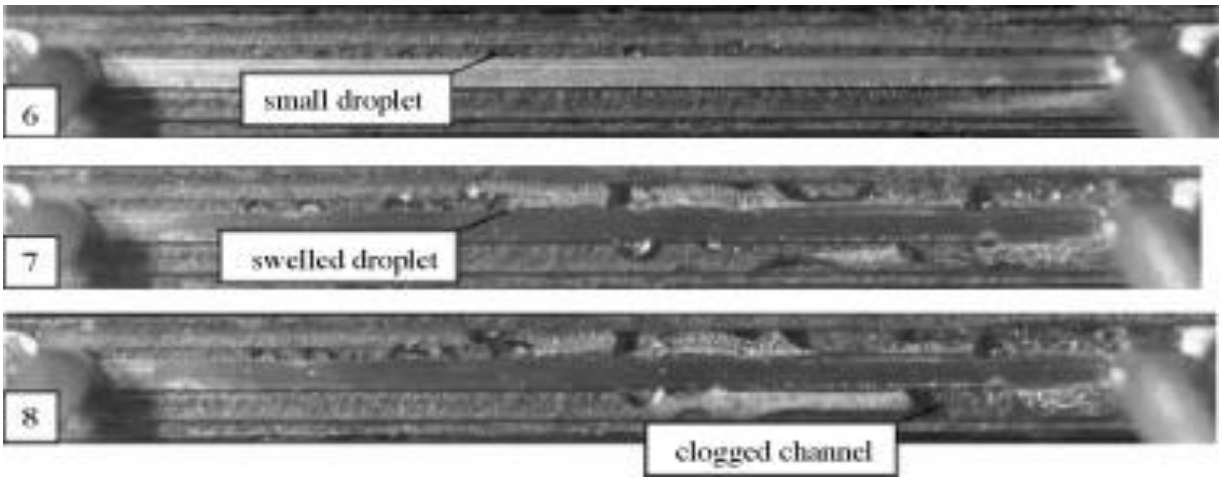

Figure 4: Water flooding in PEM fuel cell gas channels [8].

Gas flow pressure drop can be used as an indicator to measure how much water is produced in the channel. A high volume fraction of water will increase the total pressure drop across the channel. Liquid slugs temporarily blocking the channel will cause a pressure spike. In addition, pressure drop signal can be used as a diagnostic tool: the increase in the pressure drop may be correlated to decrease in the cell voltage, which signals the flooding status in the gas channels. Several studies have applied pressure measurement to identify flooding in PEM fuel cells [11-13].

Two-phase flow phenomenon is intricate in PEM fuel cells so that ex-situ studies are necessary to decouple the reactions, heat transfer and species transport from this complex two-phase phenomenon and to only focus on the two-phase flow dynamics problem. In ex-situ experiments, flow patterns are investigated under flow conditions related to fuel cell operation. The flow patterns are dependent on the superficial gas and water velocities and the geometry and

surface wettability of the gas channel. In the literature [121], several researchers observed the flow regimes as shown in Fig. 5, such as slug flow, film flow and their transitions. Mist flow can be found under a very high ratio of the gas to liquid velocity. It is an effective way to remove byproduct water, however, it is not applicable due to its high parasitic power on the pump side. A favorable flow pattern is stable film flow because liquid water transports along the channel wall with minimal blockage of the reactant gas.

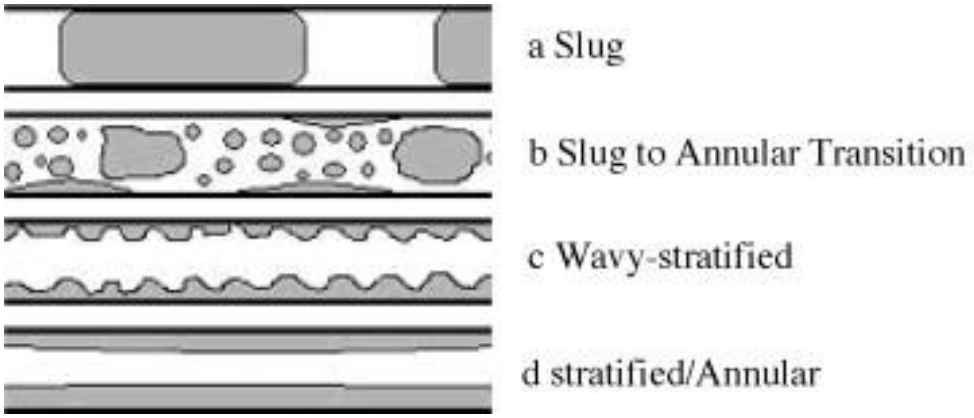

Figure 5: Flow patterns in ex-situ experiments [121].

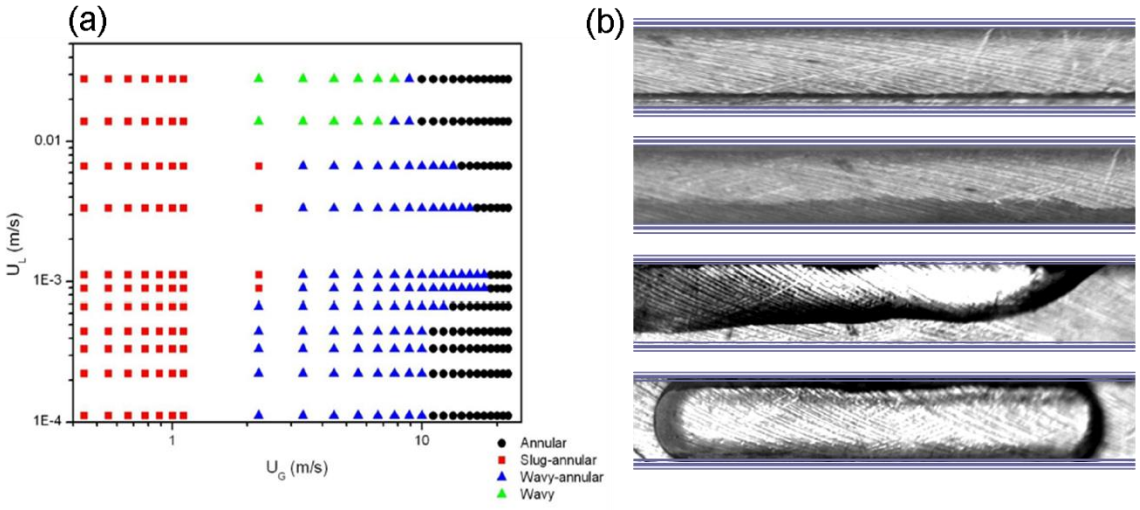

Figure 6: Flow patterns of two-phase flow in the straight channel (a); From the above to the bottom, the patterns are annular, wavy-annular, wavy, and slug-annular flows (b) [21].

Many works have been attempted to understand the complex two-phase flow in mini/micro-channels, including flow patterns, two-phase pressure drop, and phase volume fraction. Ghiaasiaan [14-15] experimentally investigated the gas-liquid two-phase flow patterns, void fraction and pressure drop in horizontal micro-channels with circular and semi-triangular cross-sections at a variety of superficial gas and liquid velocities. Kawaji [16] studied the channel diameter's impact on two-phase flow, indicating that flow patterns in the channels of a diameter less than 100 μm are different from those in mini-channels due to viscous and surface tension effects. Serizawa [17] studied the flow patterns in circular tubes of 20, 25 and 100 μm for steam–water flow in a 50 μm circular tube at a broad range of superficial gas and water velocities. He concluded that two-phase flow patterns are sensitive to the surface conditions of the inner wall of the test tube. Cubaud [18] experimentally investigated the two-phase flow in micro-channels with surface modifications and found that reduction in the channel size dramatically enhanced the wall's effects on two-phase flows. Adroher and Wang [21] investigated the patterns of air-liquid water two-phase flow in a regular micro-channel of PEM fuel cells, indicative of the occurrence of wavy, annulus, wavy-annulus and slug-annular regimes, see Figure 6. Similar flow patterns were also observed by others [19-20]. Zhao et al. [64] experimentally investigated the flow of immiscible fluids (water and kerosene) in a micro-channel of 300 μm width and 600 μm depth. The experimental data of volume of dispersed phase were correlated as a function of $W_{e_{KS}}$. Cho and Wang experimentally and numerically studied two-phase flows in a micro-channel with hydrophilic [65] and heterogeneous [66] surfaces, and found that both surface wettability and roughness affect the location of the liquid water flow, flow patterns, and pressure drop. Lee et al. [67] experimentally investigated bubble dynamics in a single trapezoid micro-channel with the hydraulic diameter of

41.3 μm. They concluded that the size of bubble detaching the channel wall is governed by the surface tension and drag of bulk flow, and bubble frequency in the micro-channel is comparable to that in an ordinary size channel. Salim et al. [68] investigated oil-water two-phase flows in micro-channels with hydraulic diameter about 700 μm. Different flow patterns were identified and mapped with pressure drops measured. They found that the pressure drop strongly depends on flow rates, micro-channel material and first fluid injected into the micro-channel. Fu et al. [69] presented experimental investigations on Newtonian/non-Newtonian fluids two-phase flow in T-shaped rectangular micro-channels. Four flow patterns were observed for cyclohexan/carboxyl methyl cellulose (CMC) solutions, including slug flow, droplet flow, parallel flow and jet flow. In general, mist flow, droplet formation, annulus, and slug flow are frequently observed in micro-channels [70]. Moreover, two-phase heat transfer in micro-channels have also been widely studied because it is capable of absorbing large amount of heat via phase change. Bowers and Mudawar [71] explored the increased rate of heat dissipation from electronic chips using flow boiling in mini-/micro-channels. They found that the flow acceleration resulting from evaporation is a major contributor to the pressure drop in the channels, and compressibility effects are significant in the micro-channels. Peles [72] conducted experiment to investigate the mechanisms associated with microscale forced convection in boiling two-phase flow. Various flow regimes were observed, including rapid bubble growth, complete bubble flow, bubbly flow and annular flow. They found that increasing the system and pump frequencies decreases the temperature fluctuation. Cheng and Wu [73] reviewed phase-change heat transfer in micro-systems, including flow boiling and condensation in micro-channels as well as bubble growth and collapse. For boiling in micro-channels, it was found that single- and two-phase alternating flows with large fluctuation of pressure and temperature exist at low mass fluxes with a high degree of inlet subcooling.

Ravigururajan [74] conducted subcooled and saturated flow boiling experiment using a diamond-pattern micro-channel heat exchanger. They inferred that heat transfer coefficients are influenced by the flow rates, wall superheat and value of quality, and the pressure drop decreases rapidly for an increasing heat transfer coefficient. In addition, droplet formation and blockage of air flow were observed using optical fuel cell design [3, 120, 122, 123]. Theories about droplet force analysis, droplet deformation, and droplet detachment velocity were developed, along with 3D numerical and experimental validation [120].

More specifically, two-phase flow dynamics in parallel mini/micro-channels has drew attention to many researchers due to its wide application in engineering. In PEM fuel cell application, flow maldistribution impairs the cell performance dramatically by non-uniform reactant transport in gas channels, great increase of total pressure drop and local hot spots. Several attempts have been made to model and predict flow distribution in parallel channels related to fuel cell applications [43-45]. Zhang found that flow mal-distribution and flow hysteresis occur at low gas and liquid flow velocities and gravitational force shows a significant impact on the flow distribution as well as the flow hysteresis [46]. Zhang [47] also studied flow patterns and pressure drop characteristics of two-phase flow in a Y-branched parallel channel system under fuel cell related operational conditions. He concluded that even flow distribution of gas and liquid could always be achieved at sufficiently high gas/liquid velocities. S.G. Kandlikar [48] proposed a new technique to measure instantaneous flow rates through individual channels in a parallel channel array. With this method, the mass flow rate in each channel can be estimated from the measured pressure drop in the entrance region as long as the contraction loss coefficient K_c is known. Suman et al. [80] performed multiphase flow computations to examine the effects of gas diffusion layer (GDL) intrusion and manifold design on reducing flow maldistribution. They showed that two

splitter plates in the header manifold can bring down the flow maldistribution. Flow maldistribution has a great impact on the performance of micro-channel heat exchangers. Nielsen et al. [75] investigated the effects of flow maldistribution on the performance of micro-channel heat exchanger both experimentally and numerically. They found that as the variation in individual channel thickness increases the heat exchanger performance decreases significantly. Anbumeenakshi and Thansekar [76] carried out experimental investigation to analyze flow maldistribution in a micro-channel heat sink. They found that flow is more uniform with trapezoidal and triangular headers at low flow rates and with a rectangular header at higher rates. Seungwhan et al. [77] developed a heat exchanger model to study axial conduction and flow maldistribution's impact. They concluded that geometry modification of cross section and cross link in parallel channels is a solution to mitigate flow maldistribution. Wen et al. [78] studied flow characteristics in the entrance of a plate-fin heat exchanger using particle image velocimetry (PIV). They concluded that fluid maldistribution in the conventional entrance configuration is severe while the improved entrance configuration with punched baffle can effectively improve the performance of fluid flow in the entrance. Kumaraguruparan et al. [79] numerically and experimentally studied flow maldistribution in the U-type micro-channel configuration, and indicated that decrease of the cross-sectional dimension and increase of the channel length reduce flow maldistribution.

Modeling is important to two-phase flow study. Several types of two-phase models have been proposed for channel flows, including homogeneous models, separated flow models, and other physics-based formulation. For homogeneous flow models, two-phase flows are treated as a single-phase flow by using average quantities as major variables regardless of flow patterns [22-23]. Various empirical correlations using the Lockhart-Martinelli parameter, following the

Martinelli method [24], have also been proposed to investigate two-phase flow and validate experimental data [25-29]. In micro-/mini-channels, the channel space can be treated as a straight regular pore structure, thus Darcy's law applies for each phase. Two-fluid models, consisting of two sets of flow equations to describe individual phase flow, have been developed with the phase interaction described by the relative permeabilities [30-34]. Fan [35] carried out both experiments and Lattice Boltzmann simulation to study two-phase flow in micro-channels. They found flow regimes depend on the capillary number and bubble breakup is induced by the phase pressure difference. Mehdizadeh [36] simulated slug flows in micro-channels with constant heat flux using the Volume of Fluid (VOF) method and found that short slugs could significantly improve the heat transfer coefficient. Qian [37] simulated the Taylor slug flow in a micro-channel with varying cross-section and concluded that the gas slug length increases with increasing superficial gas velocity and decreasing superficial liquid velocity. Fang [38] employed VOF method to simulate the vapor-venting process in a rectangular micro-channel and found that it effectively mitigated vapor accumulation by reducing pressure drop and suppressing local dry-out. In PEM fuel cells, many researchers conducted computational modeling and simulation to study air-water two-phase flow using various methods. Early adopted approaches are the multi-phase mixture model [86-89] and multi-fluid model [91-94]. However, these models cannot identify the liquid water pattern formation. Thus, more sophisticated methods, namely, Lattice Boltzmann, Level Set and Volume of Fluid methods, capable of capturing the air-water interface are needed. VOF method [97, 98, 100] was initially implemented to study two-phase flow in various gas channel configurations of PEM fuel cells where initial water was set in the pattern of droplet or film. In in situ study, liquid water emerges into gas channels through gas diffusion layers randomly in the form of droplets. Thus, water droplet dynamics of emergence,

deformation, detachment is of great importance to understand two-phase flow in gas channels of PEM fuel cells [101-104, 106]. To consider effects of the porous micro-structure of gas diffusion layers on water transport, Niu el al. [81-85] applied VOF method to investigate two-phase flow in gas diffusion layers of PEM fuel cells. To fully couple the fluid flow with mass transport, heat transfer and electro-chemical reactions, several models have been proposed and employed to study the effects of water on many aspects of cell performance [111, 113]. In addition, several researchers [117] used the VOF method to test the effectiveness of novel GDL and channel designs. Wang [30] developed a two-fluid model to evaluate and analyze the two-phase flow in a novel porous-media flow field for PEM fuel cells. Darcy's law was applied to both air and liquid phases. One dimensional (1-D) analysis gave the two-phase pressure and liquid volume fraction as a function of a number of parameters. The model was validated against previous models and experimental data for hydrophilic micro-channels [39-40], a mixed-wettability thin channel [41], and a mixed wettability channel with a rough surface [42].

Though experimental and numerical studies have been attempted, two-phase flow in micro-channels is complex, requiring additional efforts to understand and predict. For example, the contact angle's impacts will be both scientifically and technologically interesting and valuable for two-phase flow control. Recently, two-phase flow in thin channels has attracted research attention for PEM fuel cells. The Toyota Mirai vehicles adopt an about 0.3 mm thick flow field for their fuel cell stack. The ex-situ study by Lewis and Wang [40] indicated that the two-phase flow in a thin gas flow channel remains in the stratified pattern for a wide range of fuel cell operation, see Fig. 7. This kind of film flow pattern is desirable in the fuel cell application, which mitigates occurrence of flow maldistribution and improves pressure prediction and reactant supply. This research employed the VOF method, capable of tracking the

two-phase interface, to investigate the air-liquid water flow in a thin gas flow micro-channel, including the two-phase pressure drop, flow patterns, liquid volume fraction and contact angle's impacts. The results are validated by experimental study, analytical solutions and modeling predictions. To compare the simulation results with the ex-situ study [40], the study is focused on the stratified flow pattern and the experimental operating conditions to bring insights in view of modeling on thin gas flow channels. In PEM fuel cell application, micro-channels are arranged in parallel to supply reactant gas. To extend work of two-phase flow in a single micro-channel with high aspect ratio, two parallel micro-channels have been manufactured using a high-precision CNC machine and ex-situ study of two-phase flow characteristics has been performed at a variety of operational conditions with one channel subject to single phase flow and the other falling in two-phase flow regime. The pressure drop, two-phase flow patterns, and gas flow rates in both channels are investigated.

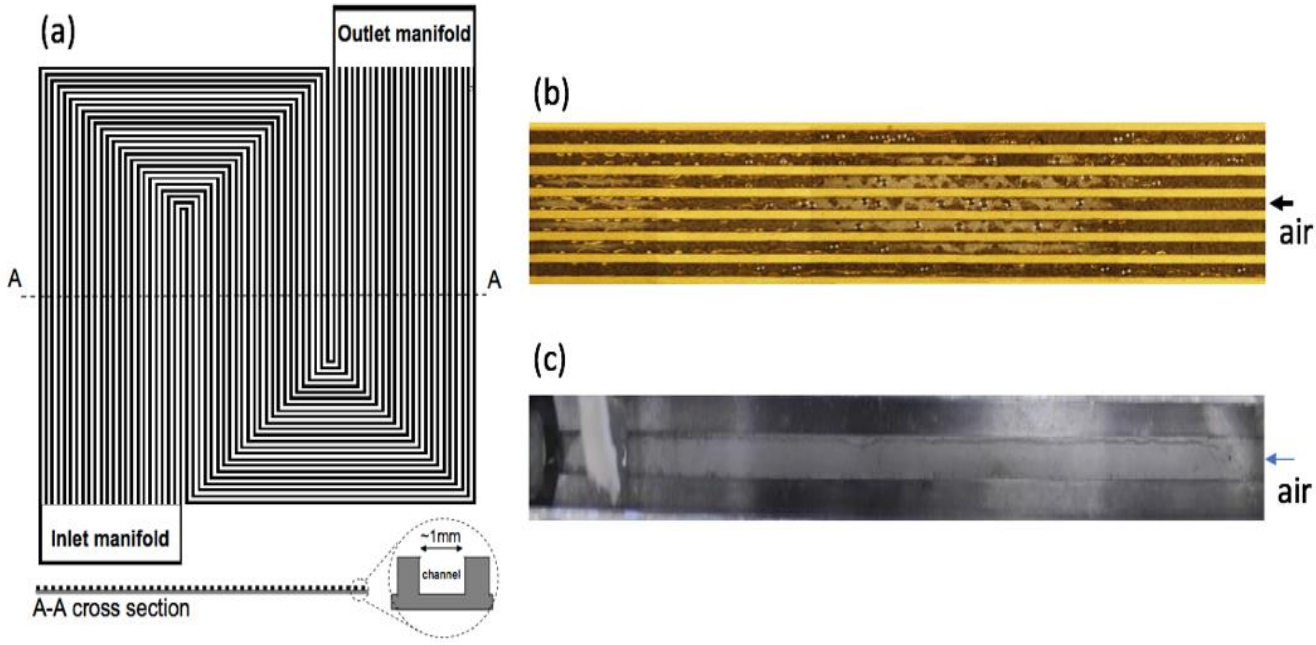

Figure 7: (a) A serpentine flow field of a PEM fuel cell; and optical visualization of: (b) two-phase flow in regular gas flow channels and (c) stratified flow observed in a thin gas flow channel [19, 40].

1.3 Objectives of the Present Study

This research work attempts to understand the two-phase flow dynamics in micro-channels under PEM fuel cell operational conditions. It is urgent to understand gas and liquid transport in micro-channels experimentally and numerically for proper water management of PEM fuel cells. To meet this need, the purpose of this study is to: 1) understand the flow dynamics problem from theoretical and modeling point of view; 2) predict the 2D/3D flow field of two-phase flow in a single micro-channel; and 3) experimentally study two-phase flow dynamics in two parallel thin micro-channels, such as flow patterns, gas flow rates in both channels, gas flow rate ratio and pressure drop.

In the following, Chapter 2 develops the theoretical results of two-phase flow in a 2D channel. Also, a two-fluid model is implemented to predict pressure field of air-water two phase flow in a single micro-channel. The modeling results are compared with simulation data and validated by experimental work. In Chapter 3, the Volume of Fluid (VOF) method with the piece-wise linear surface reconstruction technique is implemented to investigate the air-liquid water flow in a single micro-channel, including the two-phase pressure drop, flow patterns, liquid volume fraction and contact angle's impacts. Simulation results are compared with other modeling work and validated by experiment data and theoretical solutions. Chapter 4 experimentally studies the two-phase flow dynamics in two parallel micro-channels at a variety of operational conditions. The channel dimensions are the same and the operating conditions are similar as those in Chapter 3. The pressure drop, two-phase flow patterns, gas flow rates in both channels and gas flow rate ratio are investigated. Finally, Chapter 5 provides a summary and discusses future work.

Chapter 2

Theoretical Analysis and Two-fluid Model

2.1 Theoretical Analysis

2.1.1 Single-phase Flow in a Two-Dimensional Channel

Steady flow between two fixed plates with a fixed distance, h, apart is sketched in the Fig. 8. The flow is driven by a pressure gradient, $\frac{dp}{dx}$, and the body force is simply omitted. Then, the continuity equation for planar flow is:

$$\frac{\partial u_x}{\partial x} = 0 \qquad (2.1)$$

, which means u_x is only a function of y.

The planar Navier-Stokes equation for an incompressible flow with constant and uniform viscosity μ is:

$$\frac{\partial p}{\partial x} = \mu \frac{\partial^2 u_x}{\partial y^2} \qquad (2.2)$$

$$\frac{\partial p}{\partial y} = 0 \qquad (2.3)$$

Thus, p is only a function is x. Integrate both sides of the equation (2.2) so that u_x can be written as:

$$u_x = \frac{1}{\mu}\frac{dp}{dx}\frac{y^2}{2} + C_1 y + C_2 \qquad (2.4)$$

Apply boundary conditions $u_x(y = 0) = 0$ and $u_x(y = h) = 0$ to determine C_1 and C_2, then for two dimensional laminar flow:

$$u_x = \frac{1}{\mu}\left(-\frac{dp}{dx}\right)\frac{y}{2}(h - y) \qquad (2.5)$$

Then, volumetric flow rate across the channel is:

$$Q = \int_0^h \frac{1}{\mu}\left(-\frac{\Delta p}{\Delta x}\right)\frac{y}{2}(h - y)dy = \overline{u}_x h = \frac{\Delta p h^3}{12\mu L} \qquad (2.6)$$

From the equation (2.5), p is a linear function of x and the average velocity could be derived as:

$$\overline{u}_x = \frac{1}{h}\int_0^h \frac{1}{\mu}\left(-\frac{\Delta p}{\Delta x}\right)\frac{y}{2}(h-y)dy = \frac{1}{h}\int_0^h \frac{1}{\mu}\left(\frac{\Delta p}{L}\right)\frac{y}{2}(h-y)dy = \frac{\Delta p h^2}{12\mu L} \qquad (2.7)$$

Pressure difference along the x direction will then be:

$$\Delta p = \frac{12\mu L}{h^2}\overline{u}_x \qquad (2.8)$$

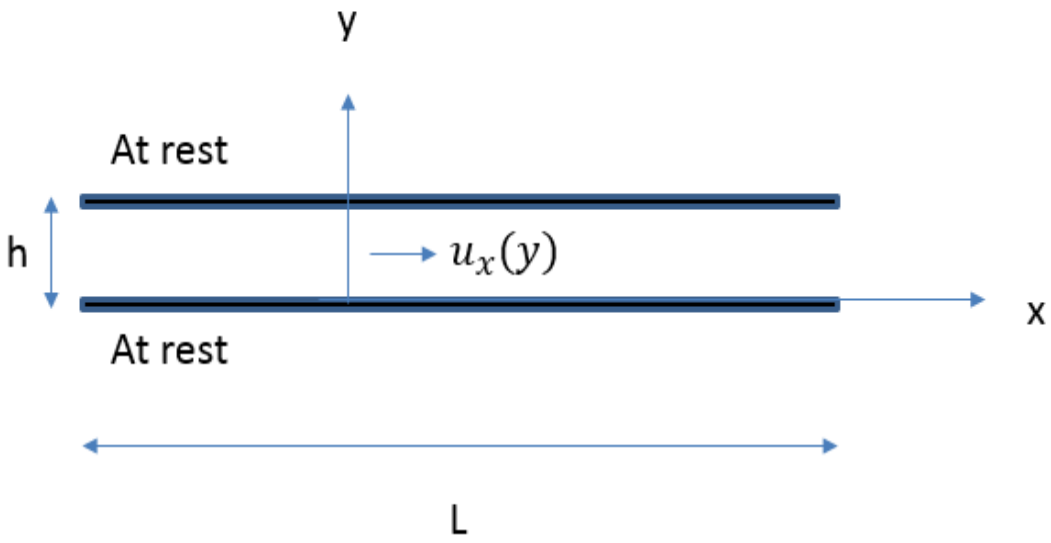

Figure 8: 2D single-phase flow field between two fixed planes.

2.1.2 Two-phase Flow in a Two-Dimensional Channel

Steady air flow between two fixed plates with a fixed distance, h, apart and water film with some thickness are sketched in the Fig. 9. The convective transport of the water is neglected. The following work treats the water species as a solid object that only occupies a certain amount of volume in the channel. Assuming the water film acting as wall and applying no slip condition to the interface of water and air:

Continuity equation: $\overline{u}_x h = \overline{u}_{x_1}(h - h_L)$ (2.9)

,where x_1 is the location of the left side of the water film and h_L is the thickness of water film.

The pressure difference across the channel is:

$$\Delta p_{2phase} = \frac{12\mu L_1}{h^2}\overline{u}_x + \frac{12\mu L_2}{(h-h_L)^2}\overline{u}_{x1} = \frac{12\mu L_1}{h^2}\overline{u}_x + \frac{12\mu L_2}{(h-h_L)^2}\frac{\overline{u}_x h}{(h-h_L)} \qquad (2.10)$$

,where L_1 is the distance between air inlet and water inlet and L_2 is the distance between water inlet and outlet.

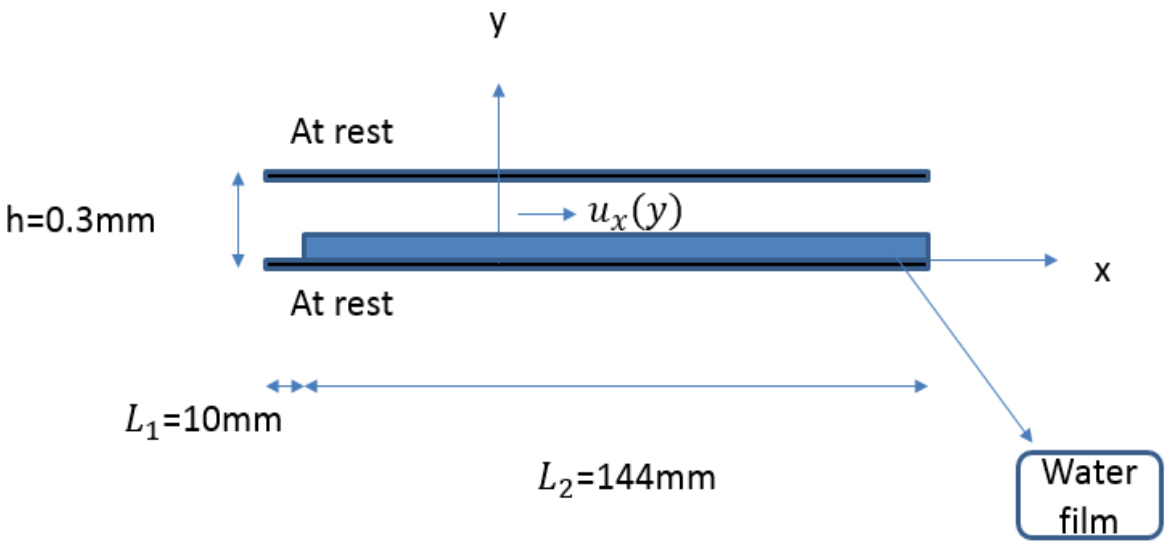

Figure 9: 2D two-phase flow field between two fixed plates.

2.1.3 Single-phase Flow in a Three-Dimensional Channel

The pressure difference (ΔP) of any pipe follows the standard relation:

$$\Delta P = \frac{fLV^2}{2D_h} \qquad (2.11)$$

,where the variables f, L, V, and D_h represent the Darcy friction factor, the channel length, the fluid velocity, and the hydraulic diameter, respectively. In general, the Darcy friction factor has the form:

$$\mathrm{f} = \frac{C}{Re} \qquad (2.12)$$

, where the constant C equals 64 for laminar flow in a circular pipe and Re is the Reynolds number based on the hydraulic diameter. In the case of a rectangular duct, the Darcy friction factor depends on the aspect ratio of the channel as

$$\mathrm{C} = 96(1 - 1.35532\alpha + 1.9467\alpha^2 - 1.7012\alpha^3 + 0.9564\alpha^4 - 0.2537\alpha^5) \qquad (2.13)$$

given by Kakac et al [49] from fitting the exact solutions of Shah and London [50] for different aspect ratios(α), where α equals the smallest dimension divided by the largest dimension.

2.2 Two-fluid Model

2.2.1 Governing Equations

Fig. 10 shows two-phase flow in the cross section of a porous-media channel. A porous medium with pore sizes of 20-100 μm and porosities of 0.9-0.95 can ensure a sufficient flow conductance. For fuel cell application, humidified air will be injected to the channel and transport towards the catalyst layer for reaction. Simultaneously, water is produced and added to the channel flow. Liquid emerges when the gas relative humidity reaches unity, leading to two-phase transport in the porous channel.

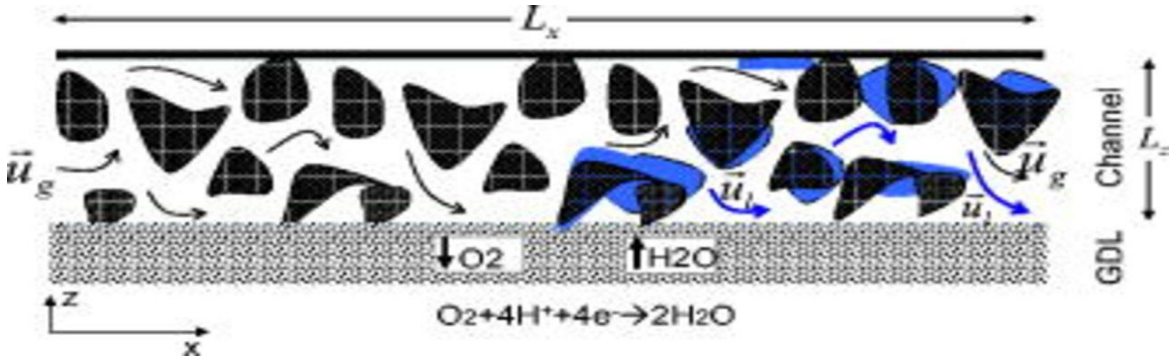

Figure 10: Cross-section of a porous channel of PEM fuel cells.

Two-fluid modeling is based on physics of fluid flows, consisting of two sets of governing equations for liquid and gas flows, respectively [39]. In Wang [30], micro-channels are treated as pore network of a structured porous medium, thus Darcy's law is applicable. By adopting the Darcy's law and neglecting the gravitational force, the momentum equations can be written in one dimension as:

Gas phase momentum conservation: $u_g = -\frac{k_{rgK}}{\mu_g}\frac{dP_g}{dx}$ (2.14)

Liquid phase momentum conservation: $u_l = -\frac{k_{rl}K}{\mu_l}(\frac{dP_g}{dx} - \frac{dP_c}{dx})$ (2.15)

,where u_g and u_l denote the superficial velocities of gas and liquid phases; $k_{rg}\ and\ k_{rl}$ are defined as the ratio of the intrinsic permeability of the gas/liquid to the total permeability of a porous medium. To simplify the above equation, one can assume the liquid transport along the channel is primarily driven by the two-phase interaction by shear stress, the capillary action is small and negligible [51].

2.2.2 Liquid Saturation Prediction of Two-fluid Model

Relative permeabilities used in the fuel cell literature are given by:

$$k_{rg} = (1 - S_e)^{n_k} \quad (2.16)$$

$$k_{rl} = {S_e}^{n_k} \quad (2.17)$$

, where effective saturation $S_e = \frac{s_l - s_{ir}}{1 - s_{ir}}$.

The value of n_k is usually set to be around 3, 4 for the GDLs (Gas Diffusion Layers) of PEM fuel cells [52,53]. However, for the study of two-phase flow in a single hydrophilic micro-channel with superficial water velocity 10^{-2} m/s and a certain range of superficial gas velocity, n_k, selected from the simulation and experimental results, is 1.159. Therefore, the above equations (2.14) - (2.17) can be resolved explicitly:

$$s_l = \frac{(\frac{u_l \mu_l}{u_g \mu_g})^{\frac{1}{n_k}} + s_{ir}}{1 + (\frac{u_l \mu_l}{u_g \mu_g})^{\frac{1}{n_k}}} \quad (2.18)$$

2.2.3 Pressure Drop Prediction of Two-fluid Model

The equations (2.16) − (2.18) could be further substituted to the pressure equations:

$$P_g = P_g(\bar{x}^*) - L_x \int_{\bar{x}^*}^{\bar{x}} \frac{u_g \mu_g}{k_{rg} K} dx \quad (2.19)$$

$$P_l = P_g(\bar{x}^*) - L_x \int_{\bar{x}^*}^{\bar{x}} \frac{u_g \mu_g}{k_{rl} K} dx \quad (2.20)$$

The total pressure drop of the gas-phase scaled by single phase flow pressure difference along the porous channel will be:

$$\Delta \overline{P_g} = \frac{\Delta P_g}{\mu_g u_{g,in} L_x / K} = \int_0^{\bar{x}^*} \frac{u_g}{u_{g,in}} dx + \int_{\bar{x}^*}^1 \frac{u_g}{u_{g,in}} \frac{1}{k_{rg}} dx \quad (2.21)$$

Assuming a constant air superficial velocity along the channel, the pressure scale becomes the pressure drop for single-phase flow. The above equation can further be rearranged as:

$$\Delta\bar{P}_g = \bar{x}^* + \int_{\bar{x}^*}^{1} \frac{1}{k_{rg}} dx \qquad (2.22)$$

Fig. 11 presents the comparison of modeling data, simulation results and experimental data for the two-phase flow in a single micro-channel at superficial water velocity 0.01m/s and a variety of air velocities.

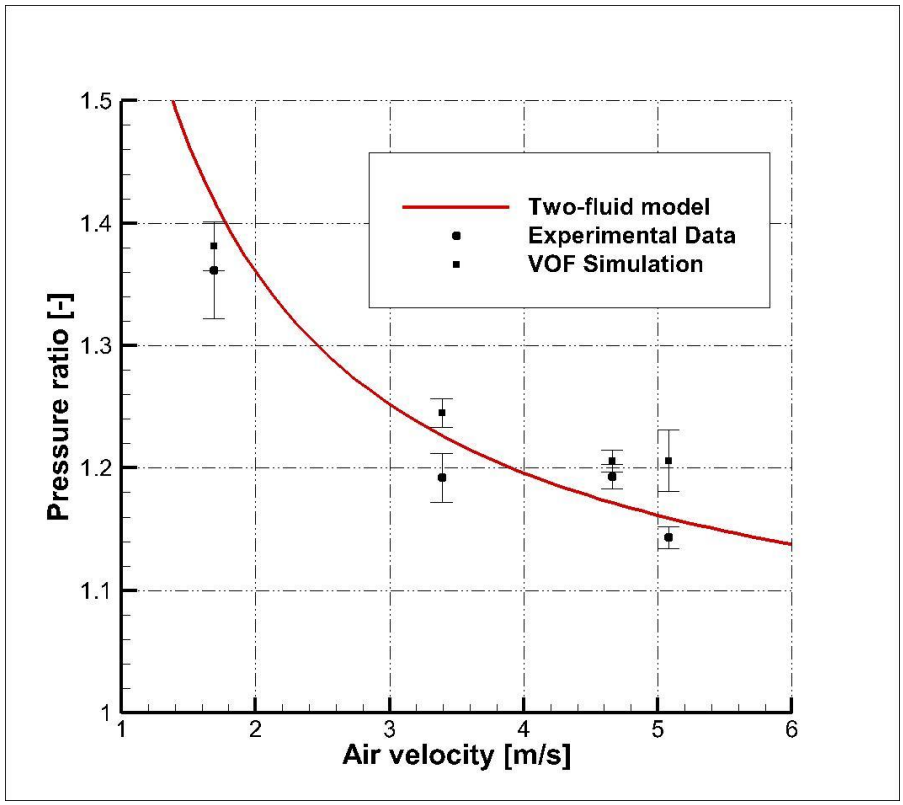

Figure 11: Comparison of predicted pressure ratio by two-fluid modeling with VOF simulation and experimental results.

Chapter 3

Volume of Fluid Simulation of Two-phase Flow in Micro-channels

3.1 Introduction

Volume of Fluid method (VOF), first proposed by Hirt and Nichols [54], is used to calculate volume fraction of each individual fluid in the fluid domain. Moreover, a surface reconstruction technique is implemented to provide accurate interface location at any instantaneous time. A single set of Navier-Stokes equations is solved simultaneously throughout the domain to obtain velocity and pressure field shared by phases. Researchers applied this method in a wide range of field of study. Typical applications include the prediction of jet breakup, the motion of large bubbles in a liquid, the motion of liquid after a dam break and the steady or transient tracking of any liquid-gas interface [55]. The objective of simulation study is to explore two-phase flow dynamics in 2D/3D micro-channels under PEM fuel cell operational conditions. Current focus is put on film flow pattern since this kind of flow pattern is desirable in the fuel cell application, which mitigates occurrence of flow maldistribution and improves pressure prediction and reactant supply. This study employed the VOF method, capable of tracking the two-phase interface, to investigate the air-liquid water flow in micro-channels, including the two-phase pressure drop, flow patterns, liquid volume fraction and contact angle's impacts. In addition, the work of this chapter is to investigate the two-phase flow in a single channel in detail, which will be applied to the design and experiment of the two-channel system, to be introduced in the Chapter 4. Specifically, the channel dimension and the ranges of the superficial liquid and gas velocities that the two-phase flow operates under the film pattern will be important inputs in the two-channel system design and experiment.

3.2 Volume of Fluid Method

3.2.1 Volume of Fluid Formulation

Volume of fluid formulation relies on the fact that any two of the phases are immiscible. In any control volume, the volume fractions of all the phases must add up to 1. More importantly, all the field variables and properties are shared by all the phases based on volume-averaged values, which depends on the volume fraction values. If the i_{th} fluid volume fraction is denoted by C_i, there are three possible conditions:

$C_i = 0$, when the control volume contains no i_{th} fluid.

$C_i = 1$, when the control volume contains full of i_{th} fluid.

$0 < C_i < 1$, when the control volume contains interface between the i_{th} fluid and one or other fluids.

3.2.2 Volume Fraction Equation

Volume fraction equation is derived from the fact that mass of volume fractions of any phases are conserved in the control volume. For the i_{th} fluid, the equation is given in the following:

$$\frac{\partial C_i \rho_i}{\partial t} + \nabla \cdot \left(C_i \rho_i \mathbf{u} \right) = 0 \qquad (3.1)$$

Moreover, the sum of the volume fractions of all phases is 1:

$$\sum_{i=1}^{m} C_i = 1 \qquad (3.2)$$

, where m is the number of phases.

For air and water flow in the micro-channel, $i = 1, 2$, where 1 denotes air and 2 denotes water. The density of these two phases remains the same everywhere all the time, so that the above two equations (3.1) and (3.2) are reduced to:

$$\frac{\partial C_i}{\partial t} + \nabla \cdot (C_i \mathbf{u}) = 0 \qquad (3.3)$$

$$C_1 + C_2 = 1 \quad (3.4)$$

3.2.3 Explicit Approach to Solve the Volume Fraction Equation

Finite-difference interpolation schemes are used to calculate the volume fraction values at the current time step from those values at the previous time step:

$$\frac{C_i^{n+1} - C_i^n}{\Delta t} V + \sum_f C_{i,f}^n U_f^n = 0 \qquad (3.5)$$

, where n+1 is the index for the current step, n is the index for the previous step, V is the volume of the computational cell, U_f^n is the volume flux through the face at the previous time step, $C_{i,f}^n$ is the face value of i_{th} fluid volume fraction.

3.2.4 Geometric Reconstruction

Based on the information of volume fraction at each computational cell, an interface of two fluids are constructed linearly in each computational cell [126], as shown in Fig. 12.

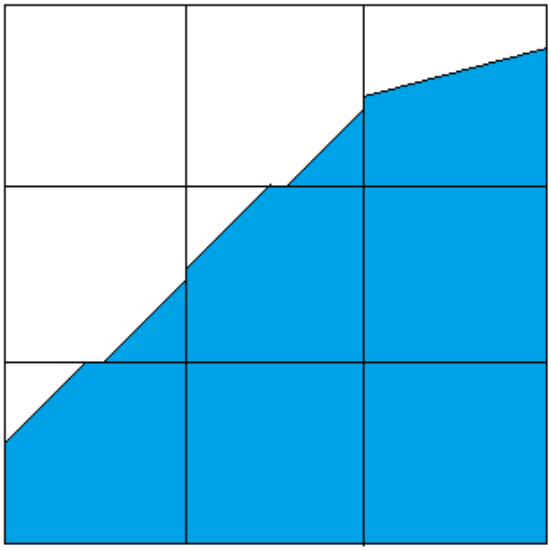

Figure 12: Linear surface reconstruction in the computational domain.

3.2.5 Material Properties

The properties such as density and viscosity appearing in the Navier-Stokes equation are determined by the volume fractional values of all the phases. In the two-phase (air and water) channel flow, if the volume of water denoted by subscript 2 is being tracked, then the density and viscosity in the computational cell is denoted by:

$$\rho = \rho_1(1 - C_2) + \rho_2 C_2 \qquad (3.6)$$

$$\mu = \mu_1(1 - C_2) + \mu_2 C_2 \qquad (3.7)$$

3.2.6 Surface Tension Effect on the Micro-channel Flow

Surface tension comes from the fact that one side of molecules are bound more tightly than the other side of molecules. In water and air flow, for example, water molecules are

connected more closely than gas molecules. This tight binding implies an additional surface energy in the free surface of water. This energy is described by the surface tension, which is defined as the amount of surface energy per unit area. Then, the unit of surface tension is N/m. Surface tension of water exposed to air is a function of temperature because intermolecular forces depend on temperature. The surface tension is balanced by the inner fluid and out fluid pressure difference, given by:

$$P_I - P_O = \sigma \left(\frac{1}{R_1} + \frac{1}{R_2} \right) \quad (3.8)$$

, where P_I denotes the pressure of fluid on the concave side, P_O denotes the pressure of the other fluid on the convex side, σ is the surface tension coefficient, R_1, R_2 are two radii of curvature in orthogonal directions. The continuum surface force (CSF) model proposed by Brackbill et al. [57] is applied to account for the surface tension effect. With this model, the addition of surface tension results in a source term in the momentum equation [55].

3.2.7 Contact Angle Effect on the Micro-channel Flow

Intermolecular forces among gas, liquid and solid will form a specific configuration of gas/liquid interface. The angle (measured through the liquid) between the tangent plane passing the interface and tangent to the solid surface at the intersection point is known as contact angle. If the water is considered as liquid phase and exposed to the ambient air, then, the contact angle is less than 90 degree, solid material in contact is characterized as hydrophilic. Otherwise, it is considered as hydrophobic.

3.3 Mathematical Model

3.3.1 Governing Equations

In the gas flow channel of a PEM fuel cell on the cathode side, the two-phase flow refers to liquid water and air flow. A VOF method is adopted to describe the individual flows with the interface of the two phases tracked by using the phase volume fraction.

a.) Governing equations

The governing equations for the two-phase VOF model in this study consist of three conservation equations [56, 124]:

Continuity equation:

$$\nabla \cdot \boldsymbol{u} = 0 \qquad (3.9)$$

Phase conservation equation:

$$\frac{\partial C}{\partial t} + \nabla \cdot (\boldsymbol{u}C) + \nabla \cdot [(1 - C)C\boldsymbol{u}_r] = 0 \qquad (3.10)$$

Momentum equation:

$$\frac{\partial \rho \boldsymbol{u}}{\partial t} + \nabla \cdot (\rho \boldsymbol{u}\boldsymbol{u}) = -\nabla \mathrm{p} + \mu \nabla^2 \boldsymbol{u} + \sigma \kappa \nabla C \qquad (3.11)$$

The physical properties of the two-phase mixture are determined by the water and air properties using their corresponding volume fractions as the weights:

$$\rho = \rho_w C + \rho_a (1 - C) \qquad (3.12)$$

$$\mu = \mu_w \mu + \mu_a (1 - \mathrm{C}) \qquad (3.13)$$

where ρ_w and ρ_a are densities of water and air, respectively, μ_w and μ_a are dynamic viscosities of water and air.

The effective velocity $\boldsymbol{u}$ and relative velocity $\boldsymbol{u}_r$ are given by:

$$\boldsymbol{u} = C\boldsymbol{u}_w + (1 - C)\boldsymbol{u}_a \qquad (3.14)$$

$$\boldsymbol{u}_r = \boldsymbol{u}_w - \boldsymbol{u}_a \qquad (3.15)$$

The continuity equation for incompressible flow applies for the air/water flow because it is under low velocity and thus the air/water density can be assumed constant. In the phase conservation equation [54], the phase fraction C takes the value of 0 or 1 if the cell is full of air or water, respectively. A value of C between 0 and 1 indicates that the cell contains an air-liquid water interface. To account for the effect of surface tension at the gas-liquid interface, the continuum surface force(CSF) model [57] is adopted to add a force source $f = \sigma\kappa\nabla C$, to the momentum equation, where σ is the surface tension and κ is the mean curvature of the phase interface given by $-\nabla \cdot \boldsymbol{n} = -\nabla(\frac{\nabla C}{|\nabla C|})$.

When the interface contacts a solid wall of a given contact angle θ, the surface unit normal $\boldsymbol{n}$ is determined by the following equation:

$$\boldsymbol{n} = \boldsymbol{n}_w cos\theta + \boldsymbol{t}_w sin\theta \qquad (3.16)$$

where $\boldsymbol{n}_w$ is the unit vector normal to the wall and $\boldsymbol{t}_w$ is the unit vector tangential to the wall.

3.3.2 Boundary/Initial Conditions

The two dimensional single channel has a dimension of 154 mm by 0.3 mm (L × h). The water inlet with the dimension of 0.3mm is located at the bottom of the rectangular domain 10mm away from the air inlet. A variety of air velocities, 1m/s, 2m/s, 3m/s, 4m/s, 5m/s and 7m/s are applied to the channel inlet, respectively, with water velocity 0.05m/s and contact angle 5 degree. Each of the two dimensional two-parallel micro-channel has a dimension of 100 mm by 0.3 mm (L × h) with shared air inlet and outlet manifolds. The superficial water velocity at bottom channel varies from 0.03m/s to 0.05m/s with air velocity 1m/s, superficial water velocity at top channel 0.05m/s and contact angle 5 degree. For the three dimensional single channel, it has a dimension of 164 mm by 3 mm by 0.3 mm (L × w × h). For the air or water inlet, an air or water velocity is set according to experimental conditions. For flow outlet,

the gradients of velocity and pressure along the channel direction are set to zero. The no-slip boundaries are imposed on the solid walls, where a contact angle θ is set as well. For no-slip boundary condition, both gas and liquid velocities are set zero at the wall surface. Initially, there is no liquid water in the channel.

3.4 Numerical Implementation

The 2D/3D single micro-channel and a 2D two-parallel micro-channel, computational flow field, were discretized using rectangular/hexahedron meshes, as shown in Fig. 13, 14 and 15. The open source software OpenFOAM was adopted to perform the numerical simulations and PIMPLE algorithm scheme, which combines the pressure-implicit split-operator (PISO) and the semi-implicit method for pressure-linked equations (SIMPLE) algorithm was used for the coupling solution of the pressure and velocity. The open-MPI was adopted for parallel computation. The time step was set 1×10^{-4} s or 5×10^{-6} s, for 2D/3D study, respectively. All the physical and model parameters for the simulation of 3D micro-channel flow are listed in Table I.

Table I: Physical properties and model parameters

Name	Symbol	Value
Air density	ρ_g	$1.19\ kg\ m^{-3}$
Liquid density	ρ_l	$998\ kg\ m^{-3}$
Air kinematic viscosity	υ_g	$1.55\times10^{-5}\ m^2\ s^{-1}$
Liquid kinematic viscosity	υ_l	$1\times10^{-6}\ m^2\ s^{-1}$
Channel dimension	-	$164\text{mm}\times3\text{mm}\times0.3\text{mm}$
Contact angle	θ	$5^{\circ}, 10^{\circ}, 20^{\circ}, 30^{\circ}, 40^{\circ}$
Surface tension coefficient	σ	7.2×10^{-2} N m^{-1}
Superficial air velocity	$\boldsymbol{v}_g$	$1.69\sim5.08\ m\ s^{-1}$
Superficial liquid velocity	$\boldsymbol{v}_l$	$5\times10^{-5}\sim1\times10^{-2}\ m\ s^{-1}$
Temperature	T	$20^{\circ}C$
Ambient pressure	P_0	1 atm
Time step in VOF	-	$5\times10^{-6}\ s$

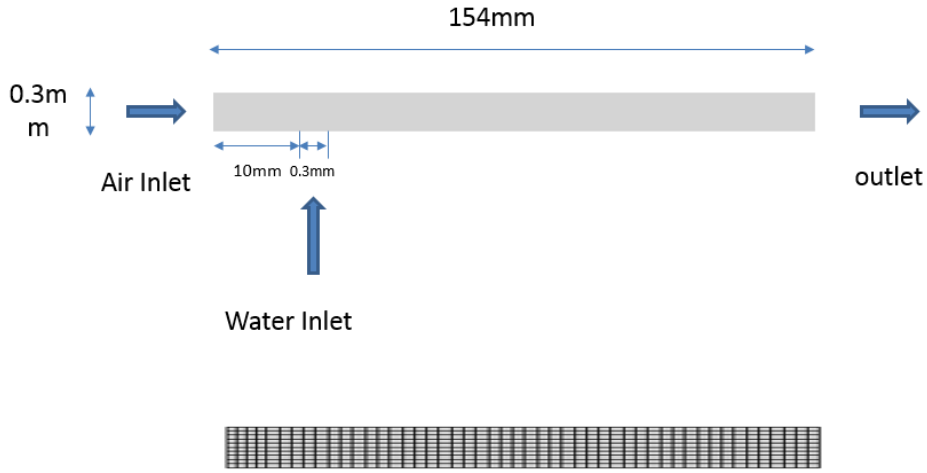

Figure 13: Computational domain of the two dimensional micro-channel.

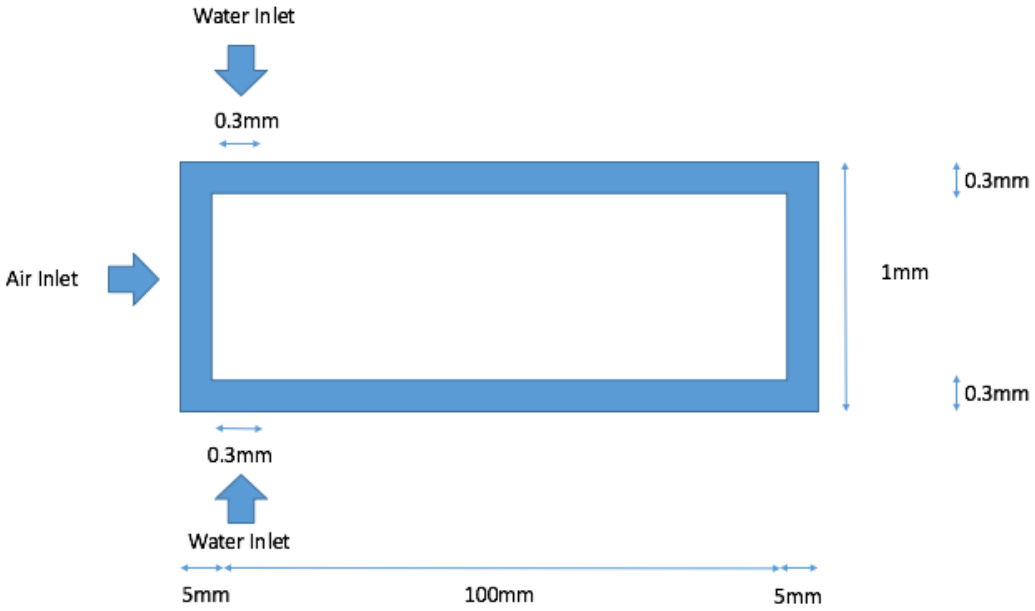

Figure 14: Computational domain of a two dimensional two-parallel micro-channel.

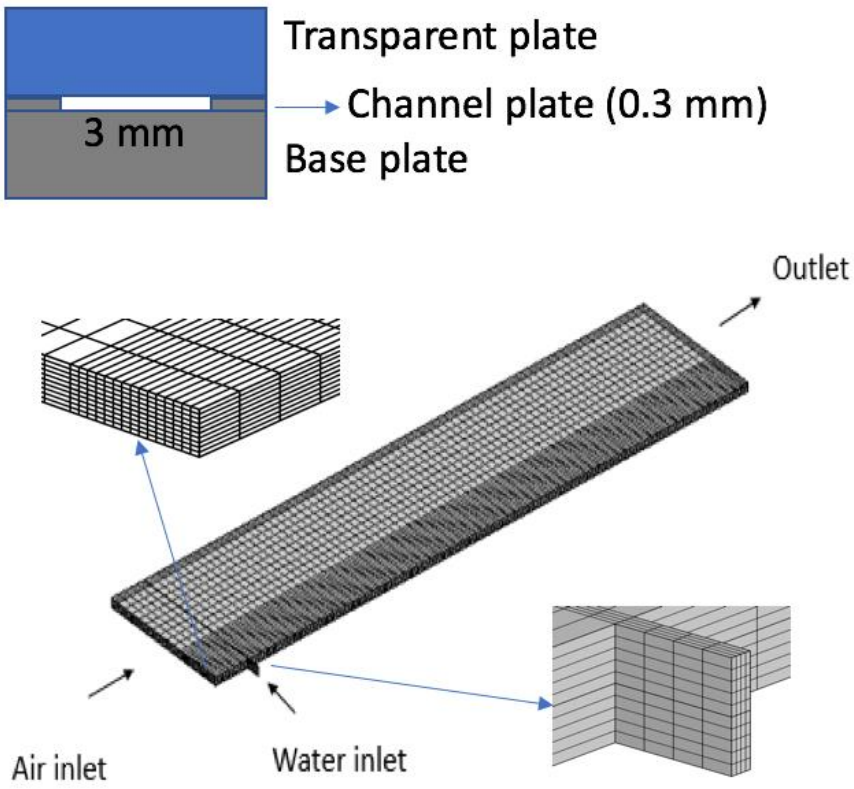

Figure 15: Computational domain of the three dimensional micro-channel.

3.5 Two-phase Flow in a Two-Dimensional Micro-channel

3.5.1 Liquid Water Flow Pattern and its Volume Fraction

Two types of flow patterns are predicted under selected boundary conditions, as shown in Fig. 16. As the air velocity varies from 1m/s to 4m/s, the wavy-film flow pattern is predicted. The VOF method predicts film flow when the air velocity falls in the range of 5m/s and 7m/s. Is is seen that water fraction decreases as the gas velocity increases. The water fraction drops significantly as the air velocity increases from 1m/s to 3m/s, then follows a slow decreasing rate, as shown in Fig. 17. It reaches as high as 0.35 at air velocity 1m/s and as low as 0.21 at air velocity 7m/s. Fig. 18 shows the time history of water fraction under given range of boundary conditions. The volume fraction still oscillates for the cases where wavy-film flow pattern is

formed. However, the amount of oscillation is almost negligible when it is compared to the total liquid fraction. The film thickness remains as constant when the air velocity is greater than 5m/s.

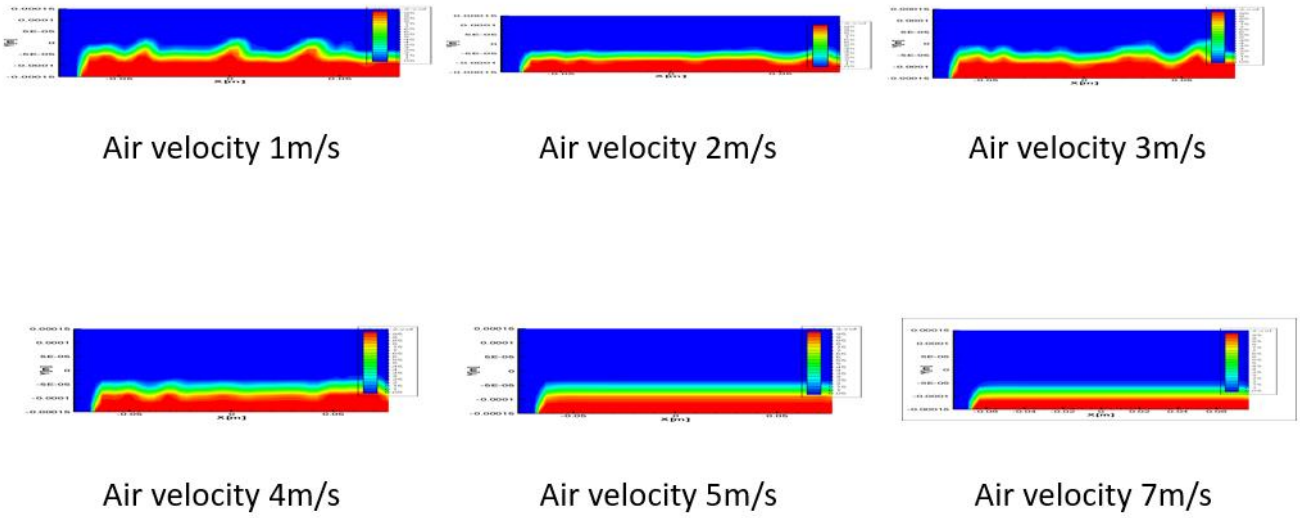

Figure 16: Water flow patterns in the 2D channel after the flow reaches steady state.

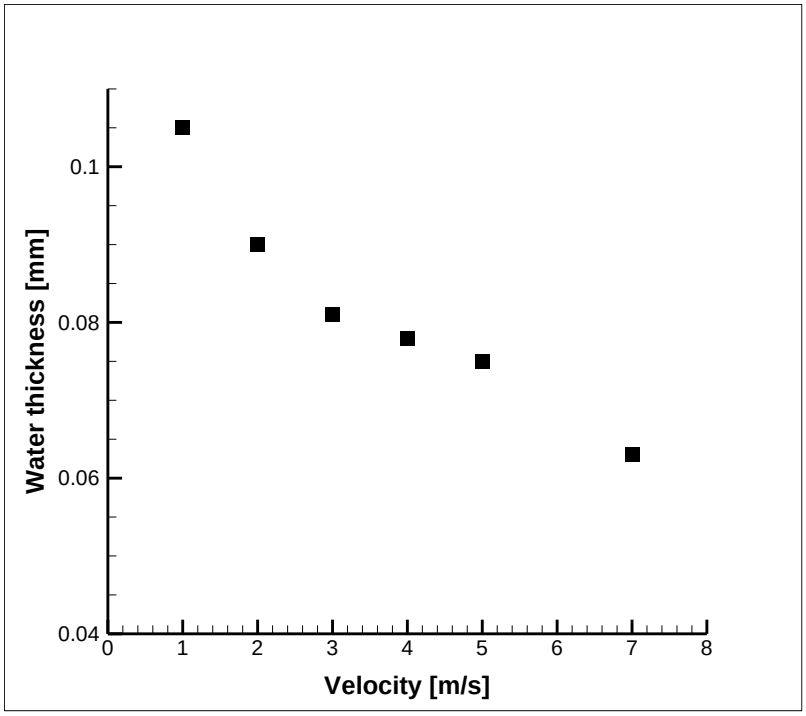

Figure 17: Water thickness at various air velocities.

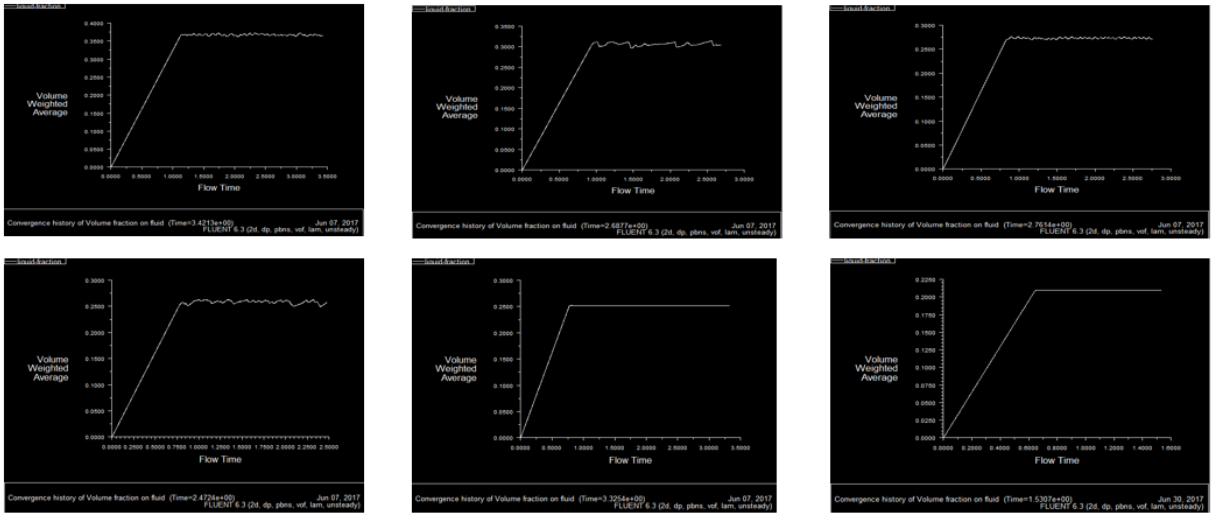

Figure 18: Water fraction vs flow time at a variety of air velocities and water velocity 0.05m/s.

3.5.2 Pressure Drop in a Two-Dimensional Channel

Fig. 19 represents the pressure history of gas phase in the two-dimensional channel. It is seen that pressure drop exhibits an oscillation for those cases where wavy-film flow pattern forms. Again, this variation is small when compared to the entire pressure drop. The gas phase pressure reaches steady state when the film flow patterns become stable at two high gas velocities. Fig. 20 shows the pressure distribution along the micro-channel when wavy-film/film flow becomes "stabilized". It is seen that pressure is almost uniform along the cross-section of the channel for all those cases of study. The pressure difference is zero across the two phases along the cross-section direction. It is mainly due to the two-dimensional channel flow where no meniscus is formed at the air-water interface. However, it may occur for the three dimensional flows.

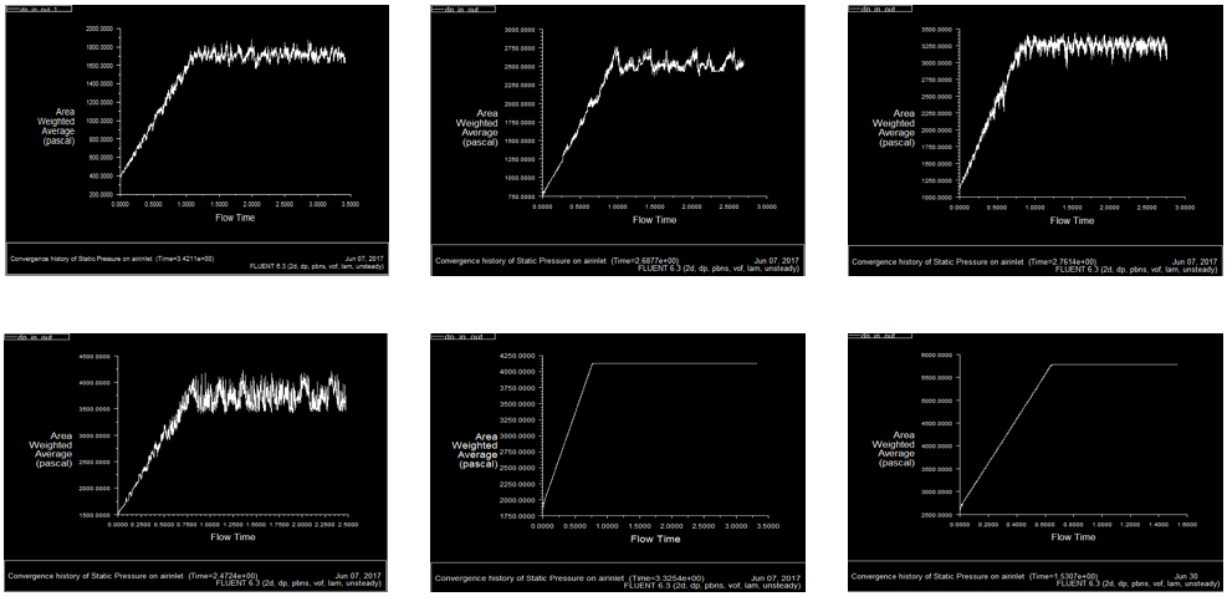

Figure 19: Pressure drop vs flow time at a variety of air velocities and water velocity 0.05m/s.

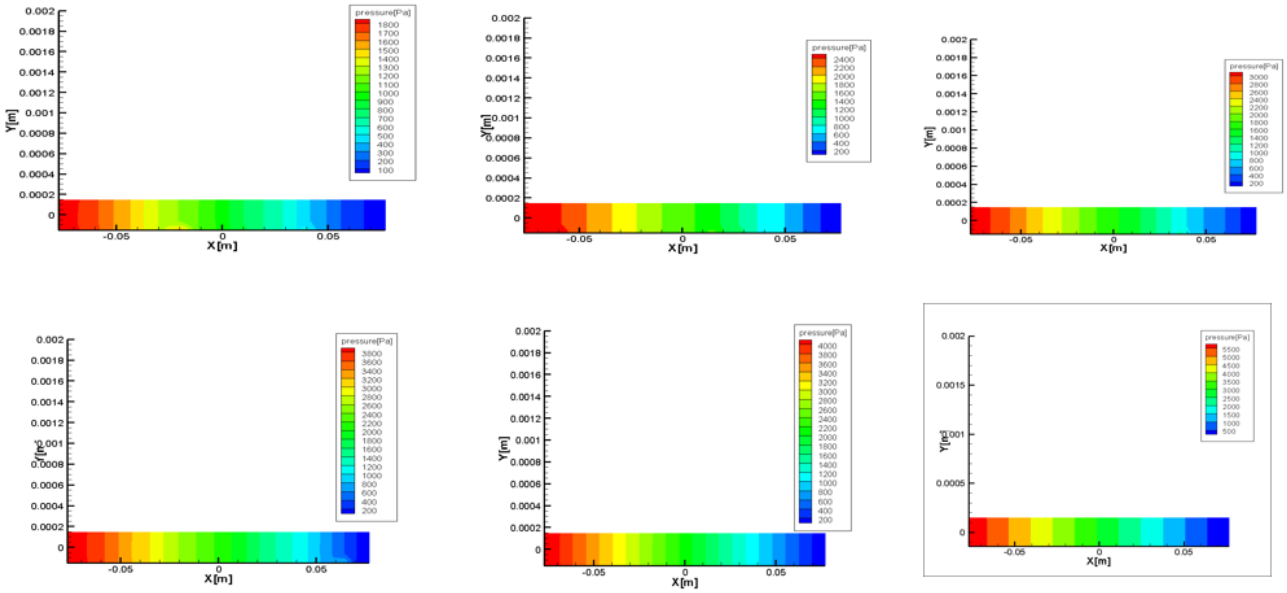

Figure 20: Pressure along the channel when flow reaches steady state.

To validate the VOF predicted gas pressure drop, the simulation data is plotted against the theory proposed in Chapter 2, as shown in Fig. 21. From geometrical dimension $L_1 = 0.01m$ and $L_2 = 0.144m$, For $\bar{u}_x$ = 1m/s, 2m/s, 3m/s, 4m/s, 5m/s, 7m/s, $h_L = 0.111 \times \frac{154}{144} mm$=0.119mm, $0.09 \times \frac{154}{144} mm = 0.096mm$, $0.081 \times \frac{154}{144} mm = 0.087$, $0.078 \times \frac{154}{144} mm$=0.083mm, $0.075 \times \frac{154}{144} mm$=0.080mm, respectively. Applying the boundary conditions, the pressure drops are determined correspondingly, namely, 1590 Pa, 2254 Pa, 2954 Pa, 3770 Pa, 4513 Pa, 5359 Pa. It is seen that the data agrees reasonably well with the theory except for the case at air velocity 5 m/s where the deviation is about 9%.

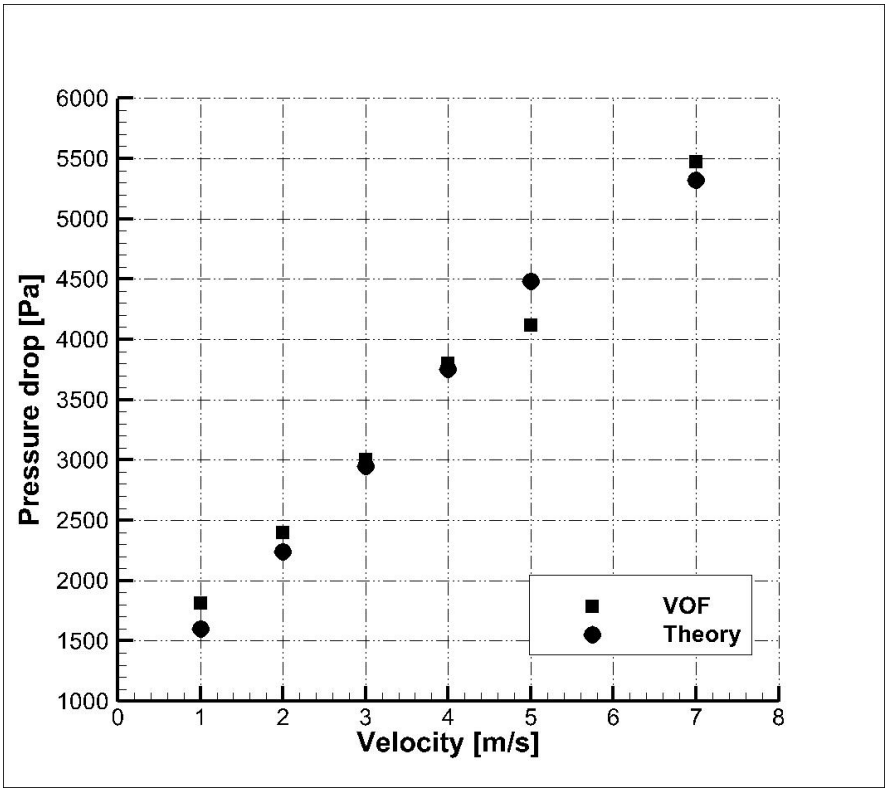

Figure 21: Comparison of theory and VOF prediction in terms of the gas pressure drop when flow reaches steady state.

3.6 Two-phase Flow in a Two-Dimensional Two-parallel Micro-channel

Case study of two dimensional flow in two-parallel channel is applied based on the fluid domain as shown in Fig. 14. A variety of superficial water velocities, namely, 0.05m/s, 0.04m/s, 0.03m/s, are applied to the bottom channel, separately, with air velocity 1m/s, superficial water velocity at top channel 0.05m/s and contact angle 5 degree. The water flow patterns and pressure drop in the two-parallel channel are shown in Fig. 22, Fig. 23. As the water velocity increases, the flow pattern in the lower channel changes from stratified flow to wavy flow film.

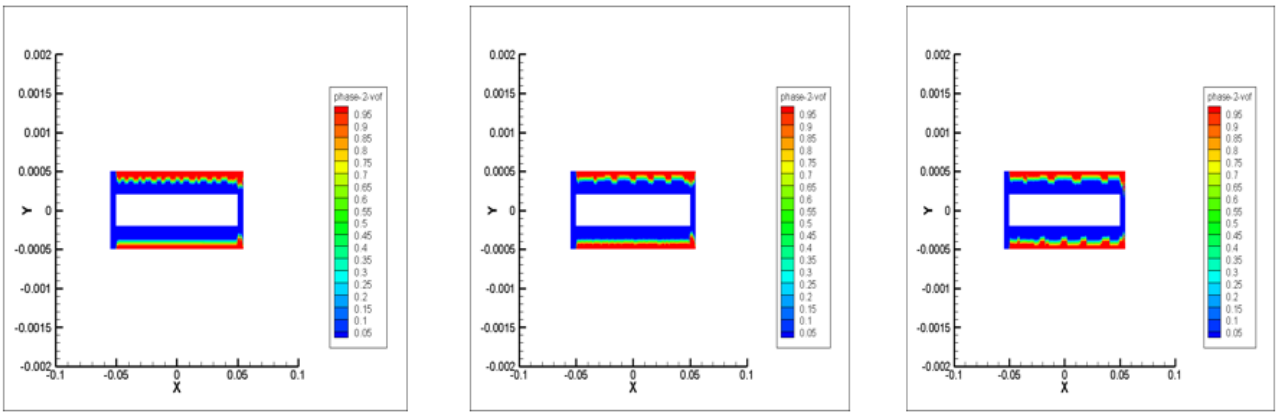

Figure 22: Water flow patterns in a two dimensional two-parallel channel

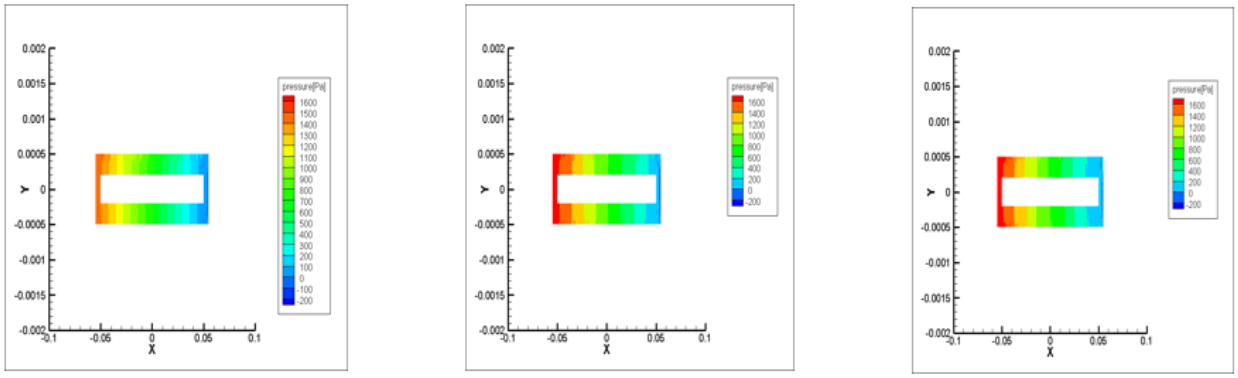

Figure 23: Pressure distribution in a two dimensional two-parallel channel

3.7 Two-phase Flow in a Three-Dimensional Micro-channel

3.7.1 Preliminary Results

A group of experimental results is selected to compare with the simulation data. The superficial gas and water velocities are shown in the Table II.

Table II: Superficial air and liquid water velocities for two-phase flow experiment in a single micro-channel

Air velocity (m/s)	Liquid Velocity (m/s)
1.69	0.01
3.39	0.01
4.66	0.01
5.08	0.01

The simulation in a 0.3mm by 3mm micro-channel model with the same boundary condition as stated in Table II. The water fraction and the ratio of two phase flow pressure drop to single phase flow are of interest to study. Fig. 24 represents the predicted film flow patterns in the 3D channel. The nodal values of water fraction at the top of the cross-section are exported for all the cases. From the case at air velocity 1.69m/s, as shown in Fig. 25, the nodal values of the third and fourth node at the top of the cross section are 0.48 and 0.005, which means interface is located between these two nodes. Then, if the water fraction is only evaluated from the top view of the channel just as how the film thickness is determined from experiment. The amount of water in the channel is overestimated. The amount of water is 20%-30% from the top view of the simulation domain which agrees well with the experimental result 21%-28%. For air velocity 3.39m/s, the volume fraction lies in 10%-20%, which is consistent with experimental data 13%-20%. At the case of air velocity 4.66m/s, the water fraction will be estimated as 10%-20% from the top view of the simulation result, which matches well with the experimental result 10%-17%.

The simulation result of the case at air velocity 5.08m/s shows 10%-20% water fraction which is in agreement with experimental result of 10%-17%.

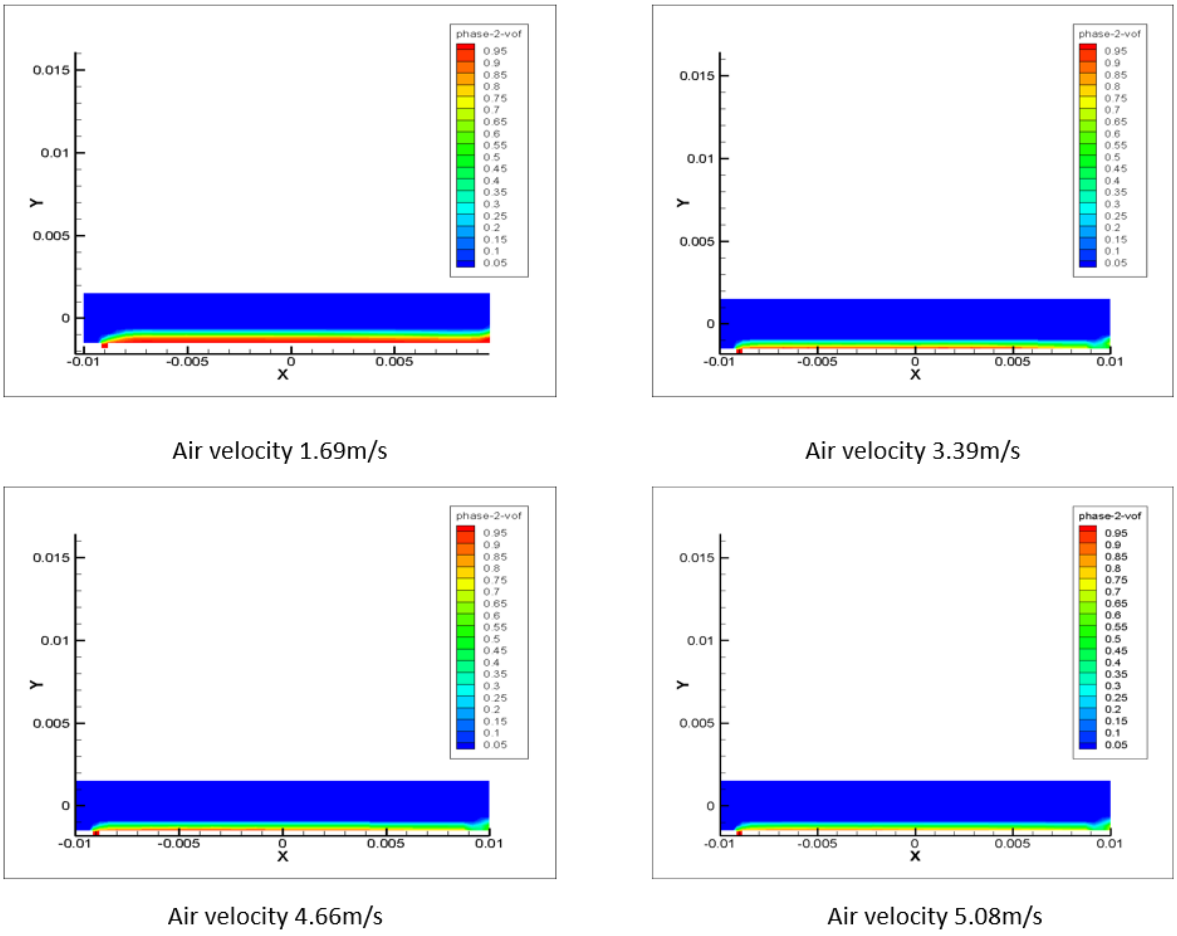

Figure 24: Water flow patterns in a 3D micro-channel

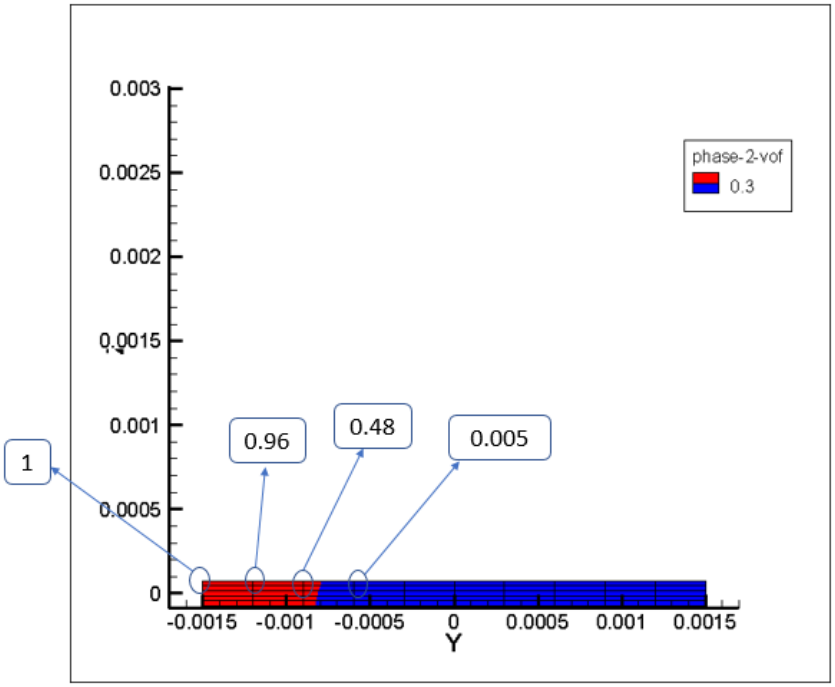

Figure 25: Water fraction in the cross-section of a 3D micro-channel at air velocity 1.69 m/s and water velocity 0.01 m/s.

The comparison of pressure ratio value from experiment with simulation is shown in the Table III and Table IV. The pressure ratio with respect to four different air velocities is shown in the Fig. 26. Note: the uncertainty of simulation is due to the pressure oscillation with respect to flow time. Each experimental data falls in a certain range due to the experimental uncertainty.

Table III: Superficial air velocity vs pressure ratio for two-phase flow experiment in a single micro-channel

Air velocity (m/s)	Pressure ratio (-)
1.69	1.32-1.40
3.39	1.17-1.21
4.66	1.18-1.20
5.08	1.13-1.15

Table IV: Superficial air velocity vs pressure ratio for two-phase flow simulation in a single micro-channel

Air velocity (m/s)	Pressure ratio (-)
1.69	1.36-1.40
3.39	1.23-1.26
4.66	1.19-1.21
5.08	1.18-1.23

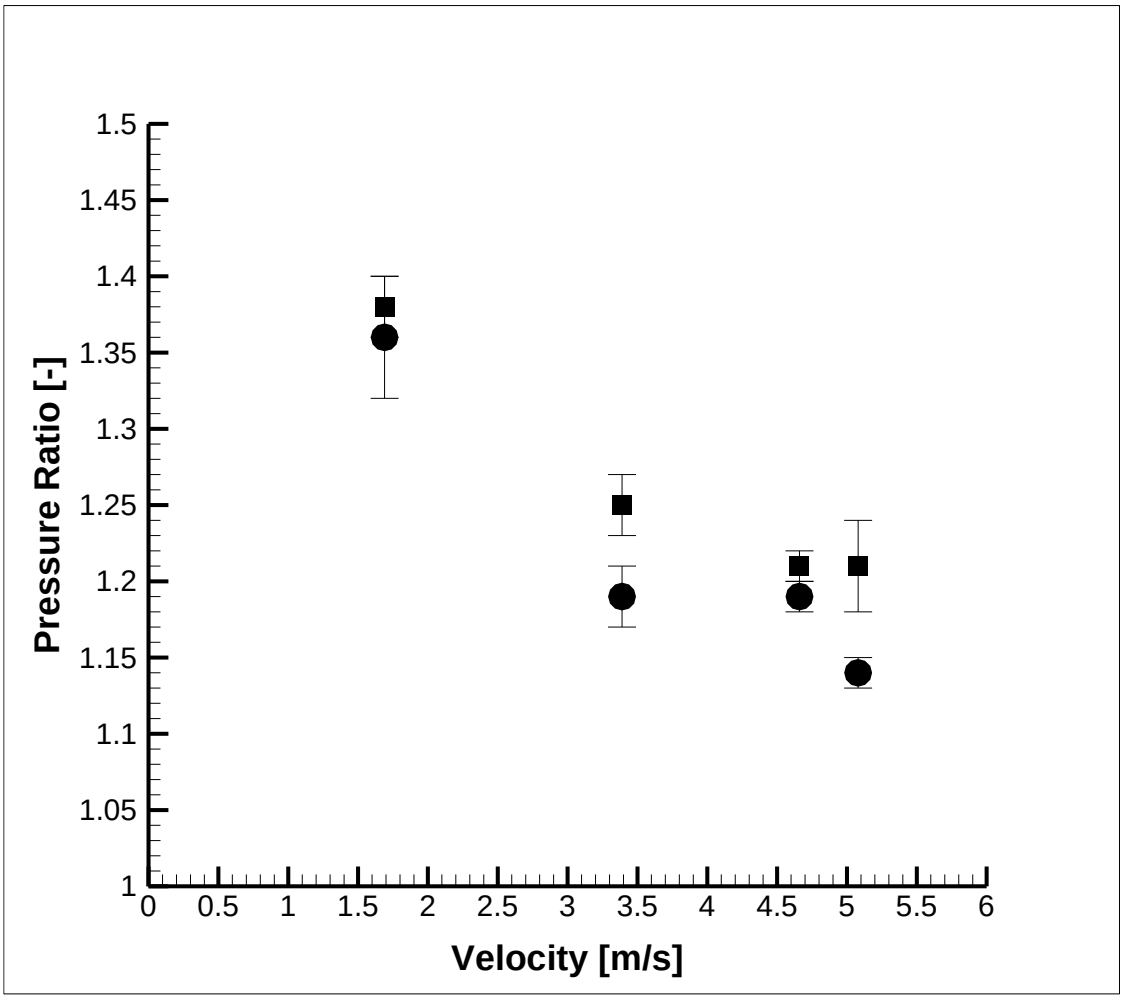

Figure 26: Comparison of experimental data and simulation results in terms of pressure ratio.

3.7.2 Liquid Water Flow Pattern and its Volume Fraction in a Single Micro-channel

Fig. 27 compares the air-liquid water interface along the channel at the superficial air velocity 1.69m/s and water velocity 0.01m/s. It is seen that a film is predicted as also observed experimentally. The predicted thickness agrees well with the experimentally determined water thickness, except near the water injection port which is set at the middle of the channel in experiment, as shown in Fig. 28. The water film remains an almost constant thickness along the channel due to no water addition or evaporation after the water injection port, and the two-phase flow remains steady possibly due to the thin channel flow where the channel wall greatly influences the flows and the two-phase interaction occurs only at the very small phase interfacial area. Because of the large impact from the wall, experimental water film has irregular pattern in local possibly due to roughness or impurity at the wall.

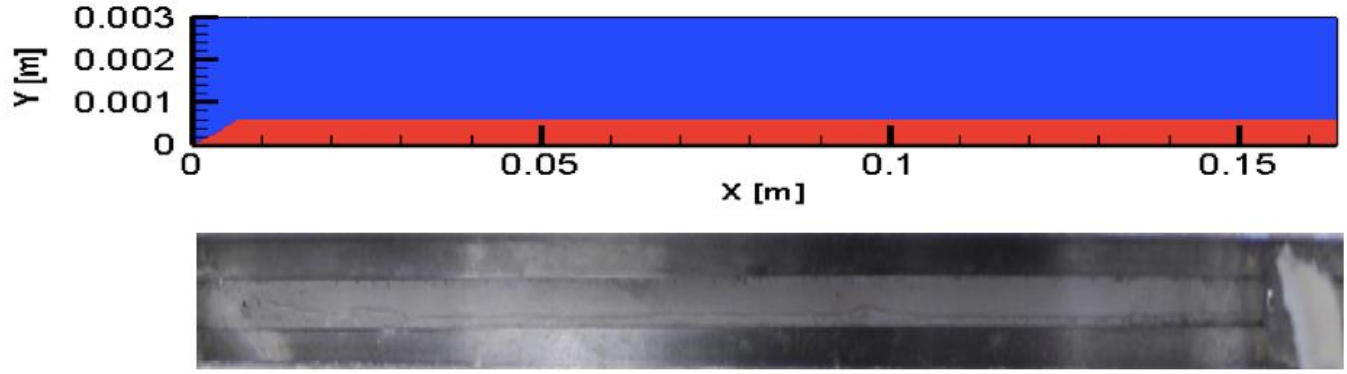

Figure 27: VOF predicted liquid water location at the transparent plate, in comparison with the experimental image of water film formation [28], at the superficial air velocity of 1.69m/s, 40° wall contact angle, and water velocity of 0.01m/s.

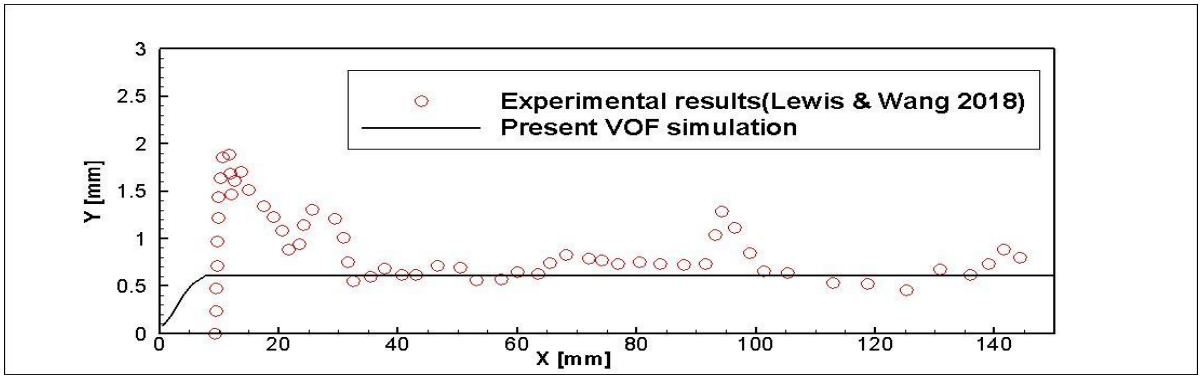

Figure 28: Comparison of the predicted water-air interface and experimental data at the superficial air velocity of 1.69m/s, 40° wall contact angle, and water velocity of 0.01m/s.

Fig. 29 compares the predicted thickness of liquid water film with experimental and other model data and analytical results. It shows that the data agree reasonably well: as the flow rate ratio increases, the liquid thickness decreases rapidly. The analytical result of Wang's model [30] is based on the exponential of the relative permeability n_k of 1.159 and refers to the liquid saturation or volume fraction in the channel. Note that the residual liquid is assumed to be zero in the simulation and analytical solutions, which may occur in experiment. In addition, in all the simulated cases film flows formed, as observed experimentally, the film thickness can be directly measured through the two-phase interface at the top wall. To compare with the experimental optical measurement, the thickness was evaluated by the liquid line at the transparent plate.

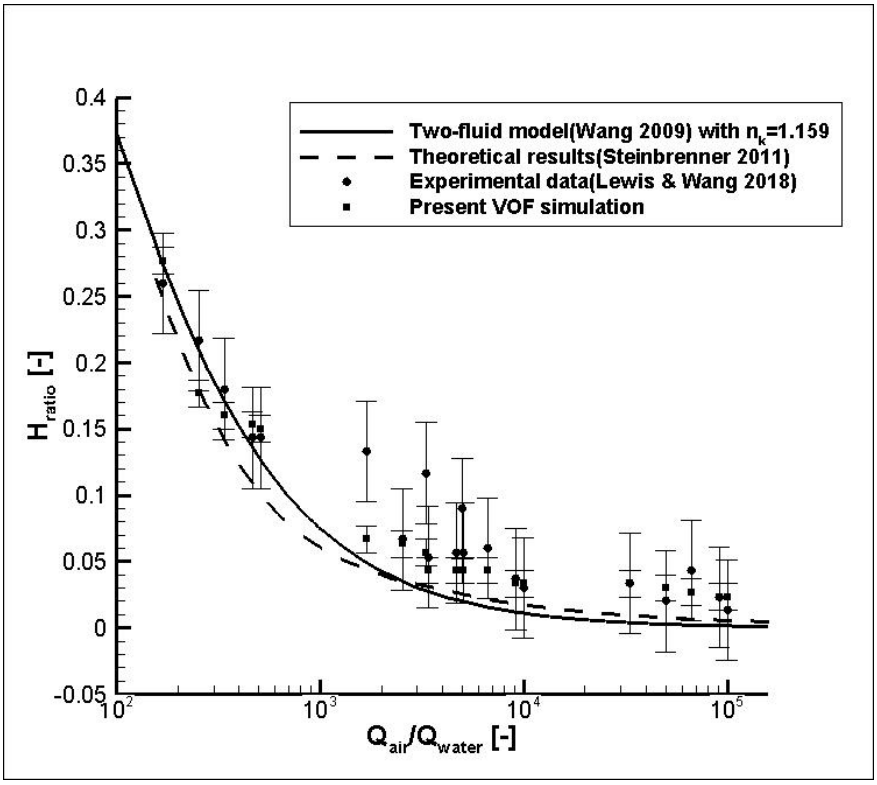

Figure 29: Comparison of VOF predicted water thickness using 40° wall contact angle with experimental, theoretical [58], and other model data.

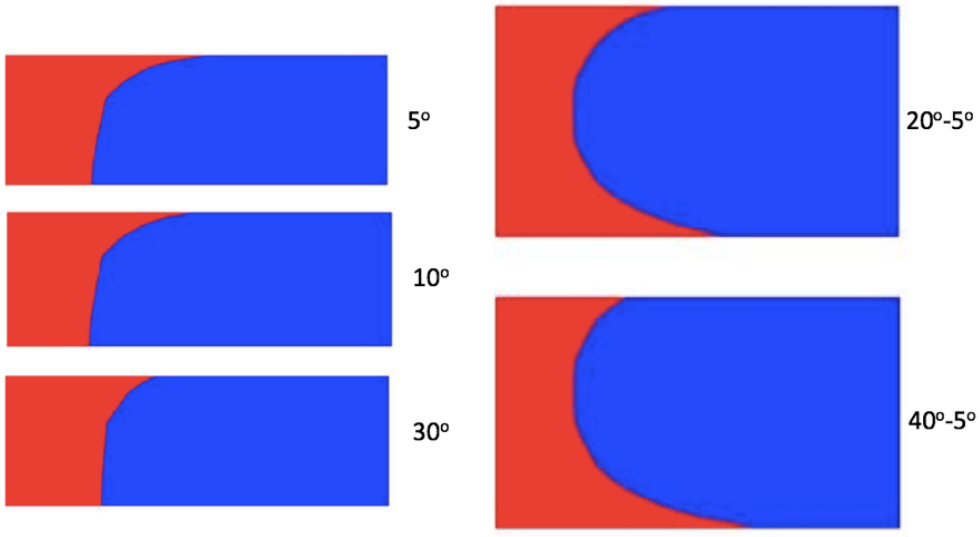

Figure 30: Predicted two-phase interface at a cross section of the channel for three contact angles (left) and two varying contact angle (right). For the left plots, the lower plane is set symmetry.

For the right plot, the above plane has a 20 ^{o} or 40 ^{o} contact angle while the rest are set at 5^{o}. The red denotes the liquid water phase and blue represents the air phase.

3.7.3 Contact Angle Effects on Two-phase Flow in a Single Micro-channel

Fig. 30. presents the two-phase interfaces at three contact angles, i.e. 5°, $10^{\circ}$and 30°. Due to symmetry, half of the channel is simulated with the bottom surface as the symmetry plane. First, it can be seen that the upper wall's contact angle changes the water-air interface in the local due to the difference in wall attraction for the three cases. The interface at the upper wall is around the specified contact angle, which is primarily due to the dominant surface tension in comparison with the forces imposed by flow and gravity, as indicated by a few dimensionless numbers for V the water velocity of 0.01 m/s: the Bond number $Bo = \frac{\Delta\rho g L^2}{\sigma} \sim 1.0 \times 10^{-2}$, the Capillary number: $Ca = \frac{\mu V}{\sigma} \sim 1.0 \times 10^{-4}$, and the Weber number: $We = \frac{\rho V^2 L}{\sigma} \sim 1.0 \times 10^{-3}$, where $\Delta\rho$ is the density difference, σ the surface tension coefficient, g the gravitational acceleration, L the characteristic length, ρ the water density and μ the dynamic viscosity of water. In addition, it is evident that the liquid water at the transparent plate is drawn up due to the hydrophilic wall. In the optical observation through the transparent plate, the water line at the transparent plate was captured as the water thickness of the channel flow, which raises uncertainty in the thickness determination due to the meniscus formation. The uncertainty in film thickness determination using the optical method is small due to the thin thickness of the channel, but could be large for a very small contact angle. For a completely wetting surface, liquid water can spread over the surface ,which makes it difficult to determine the film thickness. In addition, to facilitate optical detection one channel wall will be replaced by a transparent plate, allowing a direct observation of the two-phase flow. The transparent plate usually has a contact angle different from the base

plate. Fig. 30 (right) presents the impacts of varying wall contact angles on the interface morphology, showing that the contact angles of both the upper and lower planes affect the shape of the two-phase interface.

3.7.4 Two-phase Flow Pressure Drop in a Single Micro-channel

Due to liquid presence, the channel gas flow space narrows down, leading to a raised pressure drop. Fig. 31 presents the two-phase pressure drop along the channel versus single phase one. It is seen an almost linear drop for both single- and two-phase flow with the two-phase pressure drop larger than the single-phase one. In addition, the pressure contour indicates the pressure varies little in the direction perpendicular to the along-channel direction, similar to that of the single-phase channel flow.

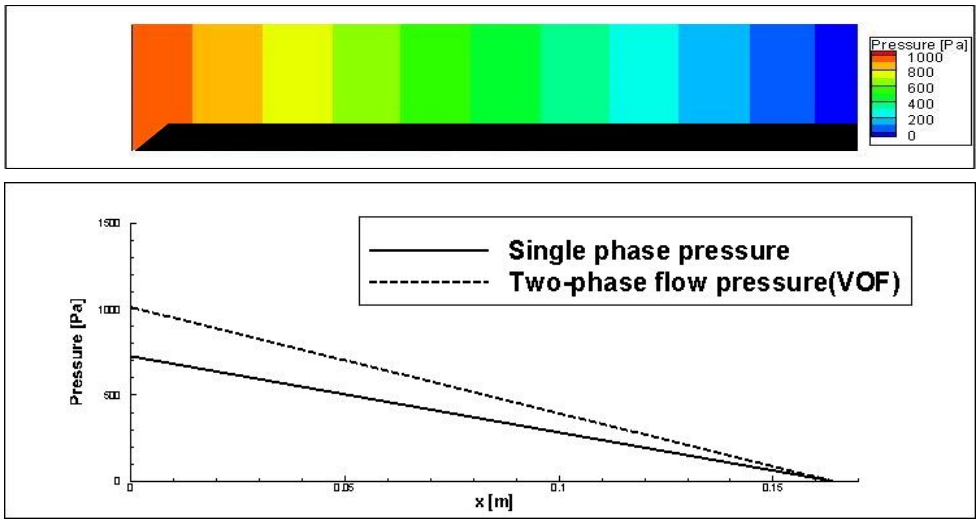

Figure 31: Predicted gas pressure contours at 40° wall contact angle (above); and gas pressure of two-phase flow along the channel (below) at the superficial air velocity of 1.69 m/s and liquid velocity of 0.01 m/s in comparison with the single-phase pressure at the superficial air velocity of 1.69 m/s.

Fig. 32 and 33 compare the predicted two-phase pressure drop with experimental data and predictions from the homogeneous, separated, and two-fluid models. It is seen that the VOF prediction agrees well with these data. Effects of the contact angle on the pressure drop are also presented, which is negligible as long as the two-phase flow remains as a steady stratified flow. For a contact angle above 40^{o}, the VOF prediction shows unstable flows in certain cases. At this stage, it is unclear the observed unstable flows are due to the VOF numerical scheme, selection of the time step, physical phenomena, or droplet attachment (residual liquid) at the wall surface [59]. The causes to instability under a contact angle over 40° are under further investigation. In addition, it is desirable to have a stable film flow in the gas flow channel of PEM fuel cells [1] because the stable two-phase flow pattern will improve pressure prediction, reactant supply and mitigate flow maldistribution among channels caused by flow pattern shift or flow instability. Fig. 34 presents the comparison of the pressure drop in channels with varying wall contact angles with experimental data. Again, the contact angle has negligible impact on the air pressure drop in the range of the selected contact angles, despite the distinct interface shape as disclosed by Fig. 30.

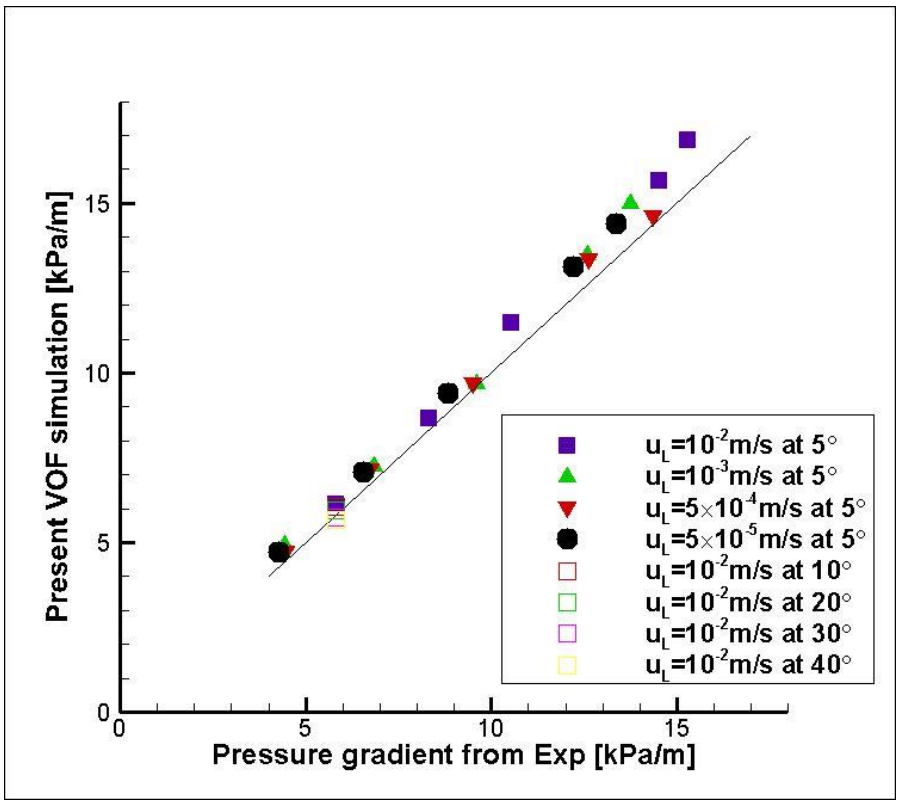

Figure 32: Predicted pressure drop using various contact angles, in comparison with experimental data [40].

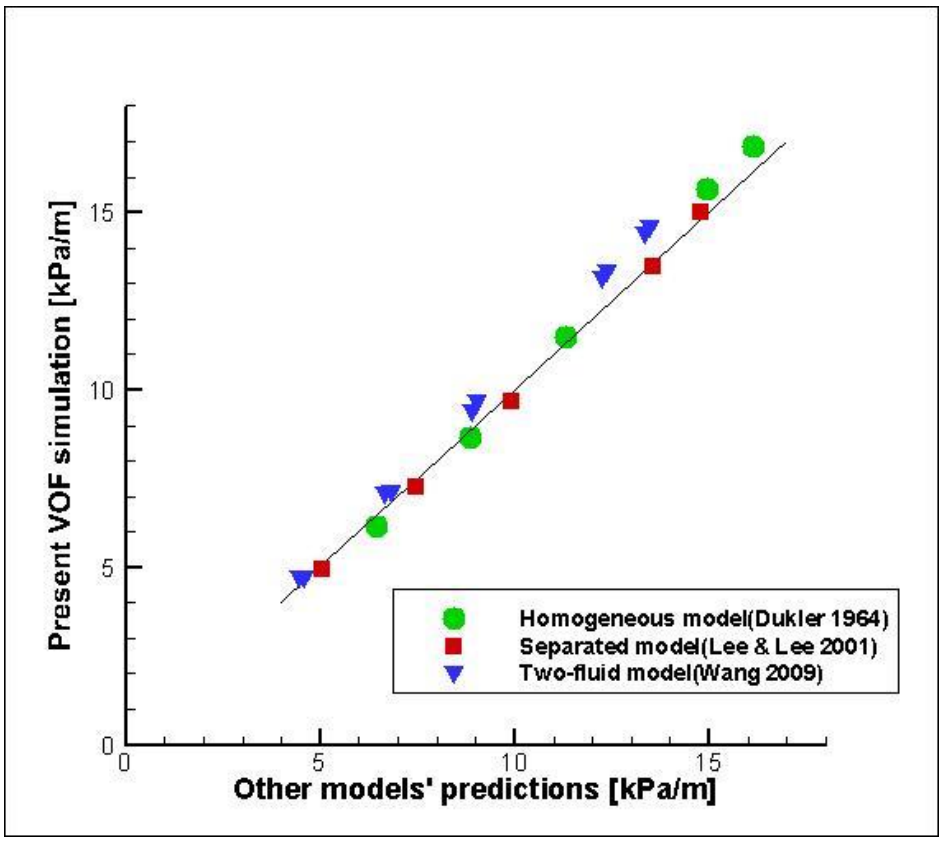

Figure 33: Predicted pressure drop of the wall contact angle at 40° in comparison with various model results [60-61].

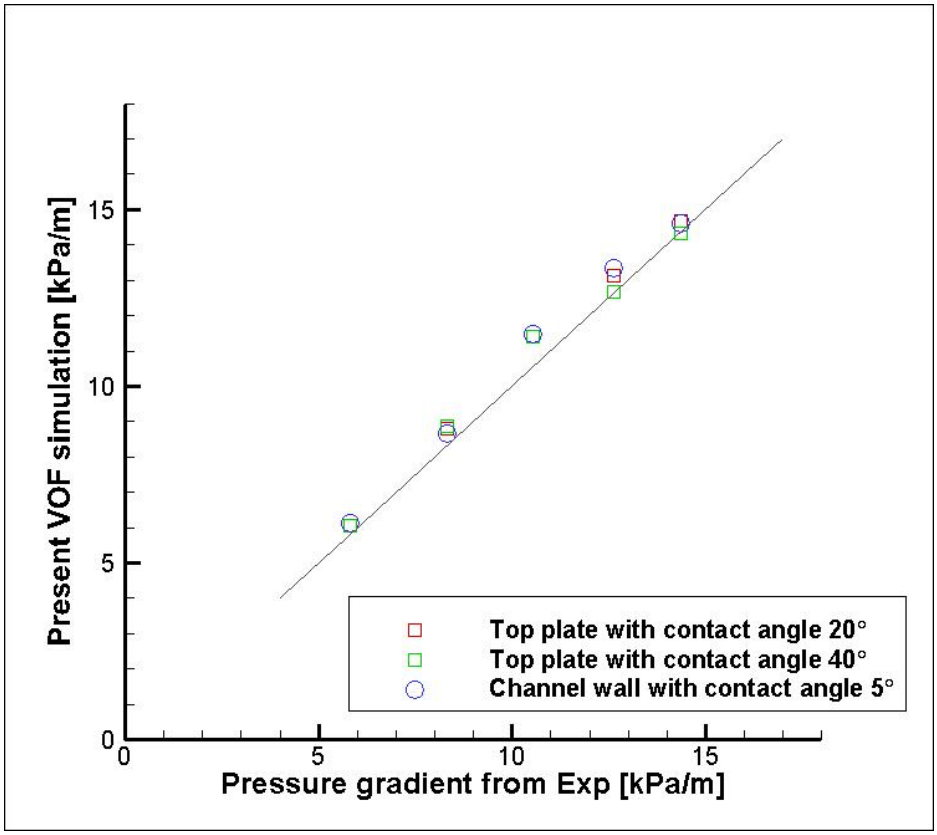

Figure 34: Predicted pressure drop in channels of varying wall contact angles in comparison with experimental data [40]. The two-phase interfaces are plotted in Fig. 30.

In this study, the VOF method was employed to investigate the two-phase flow dynamics in a thin gas flow channel in a PEM fuel cell with a dimension of 164 × 3 × 0.3 mm. Various contact angles of the channel walls were studied to investigate their impacts on the two-phase interface where the air-liquid interaction occurs, film thickness, and impacts on the pressure drop. The results were compared with various empirical models, two-fluid model, theoretical solutions and experimental results, in terms of the pressure drop, flow patterns and water volume fraction. We found that 1.) the wall contact angle impacts the two-phase interface in the thin channel by altering its curvature near the wall. The near-wall's two-phase interface shows an angle close to the wall's contact angle due to the dominant force of surface tension and wall impact. 2.) It was

indicated that the contact angle may affect the optical observation of the liquid water thickness due to the interface curvature and raise uncertainty in the method of film thickness determination. 3.) The predicted flow remains in the stratified regime, as experimentally observed, for the contact angle ranging from 5° to 40°. The water fraction agreed well with the two-fluid model, analytical results, and experimental data. 4.) The predicted gas pressure agreed well with the experimental data, two-fluid model and some empirical models. The contact angle showed a negligible impact on the predicted pressure drop in the range of 5° to 40° including varying wall contact angles, in which the VOF predicted stable water film formation. For the contact angle over 40°, the VOF predicted unstable flows. The film instability is under further investigation for future publication.

Chapter 4

Experiments of Two-phase Flow in Two Parallel Micro-channels

4.1 Experimental

4.1.1 Design of Experimental Apparatus

Fig. 35 shows the design of two-parallel thin micro-channels in experiment. It consists of two identical micro-channels arranged in parallel and placed horizontally with a shared inlet manifold and their outlets connected to the ambient air. Both channels have a rectangular cross-section of 0.324 mm by 3.00 mm with a total length of 178 mm. Note that the channel cross-sectional dimensions are the same as those in the Chapter 3. The channel plate is made of 304 full-hard stainless steel, which is placed on a 6061 aluminum base. A polycarbonate window plate is placed on top for flow visualization. All the components were fabricated using a high-precision CNC milling machine.

4.1.2 Experimental Setup

Fig. 36 schematically shows the experiment setup, including the two channels system, inlet gas flow controller, liquid injection controller, pressure measurement unit, gas flow rate measurement unit and visualization camera. Two-phase flow formation is established by injecting the water into Channel 2, while Channel 1 remains in single-phase flow in its entire length without water addition. The water injection port was a hole drilled on the base plate with a diameter of 0.28mm, located at 60 mm downstream from the inlet. Thus, Channel 2 consists of a single-phase flow before the port and a two-phase flow region after. A syringe pump (New Era Pump System NE-300) injects room temperature deionized water into Channel 2 at three flow

rates, 0.3499, 3.499, and 34.99 $ml/hour$, corresponding to a superficial velocity of 10^{-4}, 10^{-3} and 10^{-2} m/s, respectively. A mass flow controller (SmartTrak 100) regulates seven air flow rates at room temperature ($20°C \pm 2°C$) in the range of $100 - 400$ ml/min ($\pm$ 5 ml/min), corresponding to a superficial velocity of $0.86 - 3.44$ m/s. The ranges of the gas and liquid superficial velocities are selected according to those in the VOF study of Chapter 3, which shows that the two-phase flow pattern falls in the film flow regime. The inlets and outlets of the two channels share the same manifolds, ensuring that the same pressure drop for the two micro-channels.

A transducer (OMEGA PX 409) was used to measure the pressure drop between the channel inlet and outlet. The gas flow rate in each channel was measured by collecting the gas volume in a given duration. The flow patterns in the two-phase channel were captured by a DSLR camera (canon Rebel T3) when the pressure drop reaches steady state, which takes 10 min to 2 hours depending on the air and water flow rates. Table II lists the operational conditions, physical properties of fluids and channel parameters.

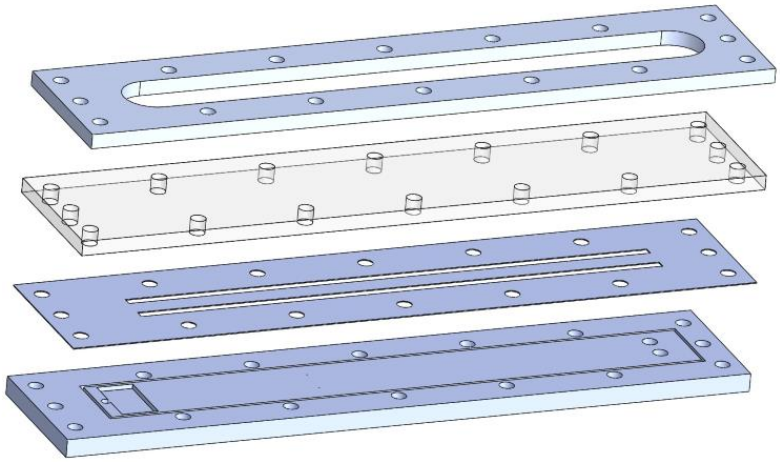

Figure 35: Design and assembly of two parallel micro-channels (From top to bottom: O-shaped endplate, transparent plate, channel plate, and base plate).

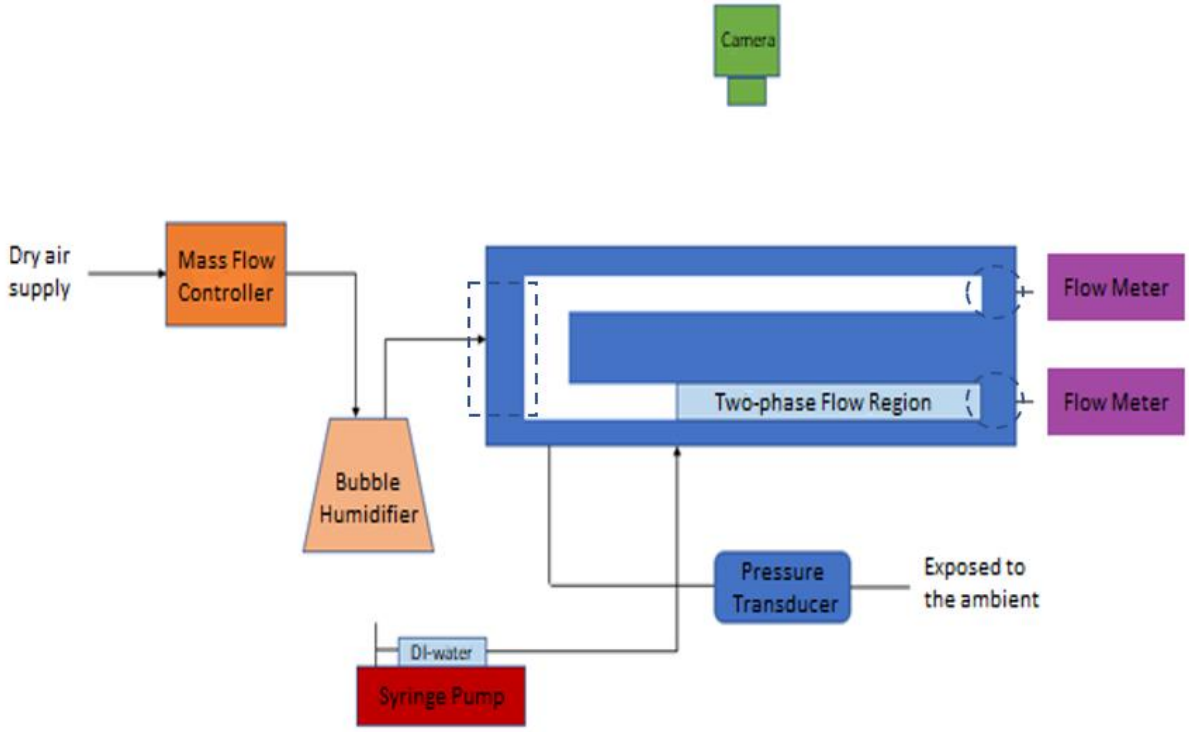

Figure 36: Schematic of the experimental test section. Channel 1 (the upper channel) is subject to single phase flow, while Channel 2 (the lower channel) is in two-phase flow regime after the liquid injection port. The port is located at the first 1/3 of the channel length.

Table V: Operational conditions of experimental testing, physical properties of fluids and channel parameters

Name	Value	Unit
Air flow rate	**100, 150, 200, 250, 300, 350, 400**	**mL/min**
Superficial air velocity	**0.86, 1.29, 1.72, 2.15, 2.58, 3.01, 3.44**	**m/s**
Water flow rate	**34.99, 3.499, 3.499× 10^{-1}**	**mL/hour**
Superficial water velocity	**$10^{-2}, 10^{-3}, 10^{-4}$**	**m/s**
Channel dimension	**$178 \times 3 \times 0.324$**	**mm**
Water port location (from Channel inlet)	**60**	**mm**
Temperature	**20**	**°C**
Ambient pressure	**1**	**atm**

4.2 Two-phase Flow of Two Micro-channels in Parallel Arrangement

4.2.1 Pressure and Volumetric Flow Rate Validation of Single-phase Flow in Micro-channels

To verify the cross-sectional areas and the identical dimension of Channel 1 and 2 in the experimental setup, single-phase flow testing was first conducted. For single phase flow in a channel [50], the static pressure drop is given by:

$$\Delta P = \frac{f L {u_g}^2}{2 D_h} \quad (4.1)$$

, where f, L, u_g, D_h represent Darcy friction factor, channel length, superficial fluid velocity and hydraulic diameter, respectively. In general, Darcy friction factor has the form:

$$f = \frac{C}{Re} \quad (4.2)$$

In the case of single phase flow in a rectangular channel [49]:

$$C = 96(1 - 1.35532\alpha + 1.9467\alpha^2 - 1.7012\alpha^3 + 0.9564\alpha^4 - 0.2537\alpha^5) \quad (4.3)$$

,where α is aspect ratio of the channel, defined as the ratio of height to width of the cross-section. The pressure drops across Channel 1 and Channel 2, respectively, are the same due to sharing of the inlet manifold and the ambient outlet. The superficial velocities are assumed the same in the two channels and then calculated by dividing the total air flow rate by the total cross-sectional area of the two channels. Fig. 37 compares the experimental data of the pressure drop with the theoretical results using Eq. (4.1). The deviation from the theoretical value is within 2% for most cases except for the case at highest velocity in which the difference is about 4%. The uncertainties in the pressure and gas flow measurements are 2 Pa and 0.043 m/s, respectively.

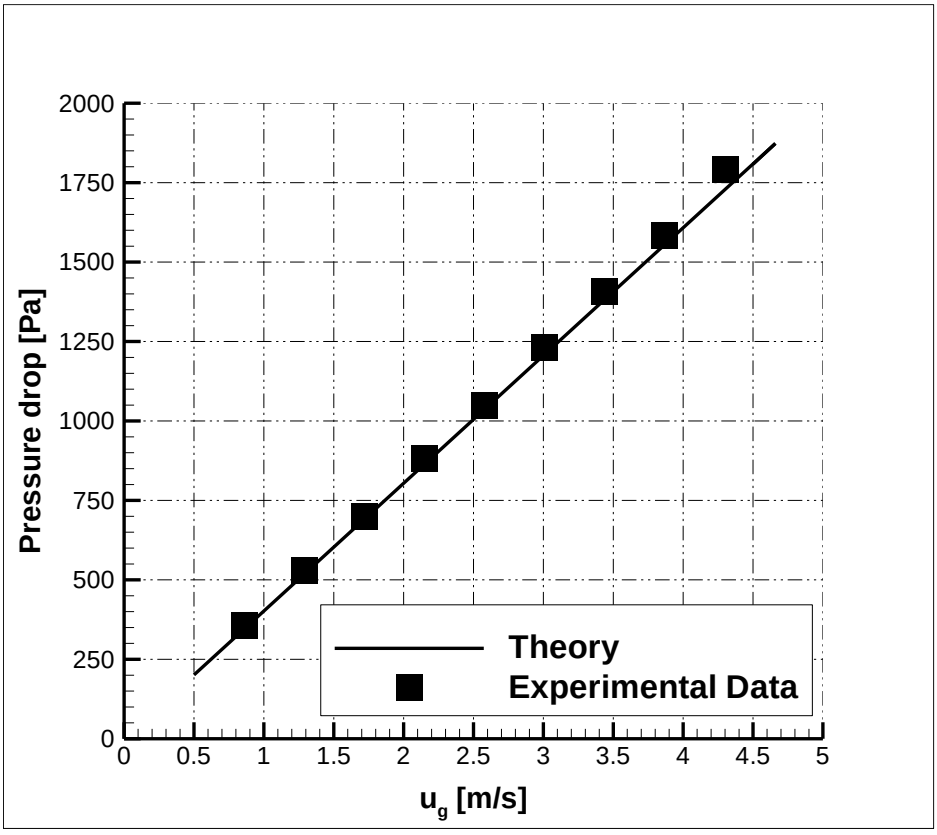

Figure 37: Gas flow pressure drop under no liquid injection condition: theoretical versus experimental data.

In order to verify the identical dimension of Channel 1 and Channel 2, the volumetric flow rates were measured simultaneously in each of the two channels at steady state. Under each condition, the measurement of air flow rate was repeated five times, respectively. Fig. 38 compares the air flow rates in two channels at four testing conditions without any water injection in Channel 2, i.e. both channels are subject to single phase flow. It can be seen that Channel 1 and Channel 2 have similar flow rates with difference less than 3%, indicative of identical dimension for the two channels.

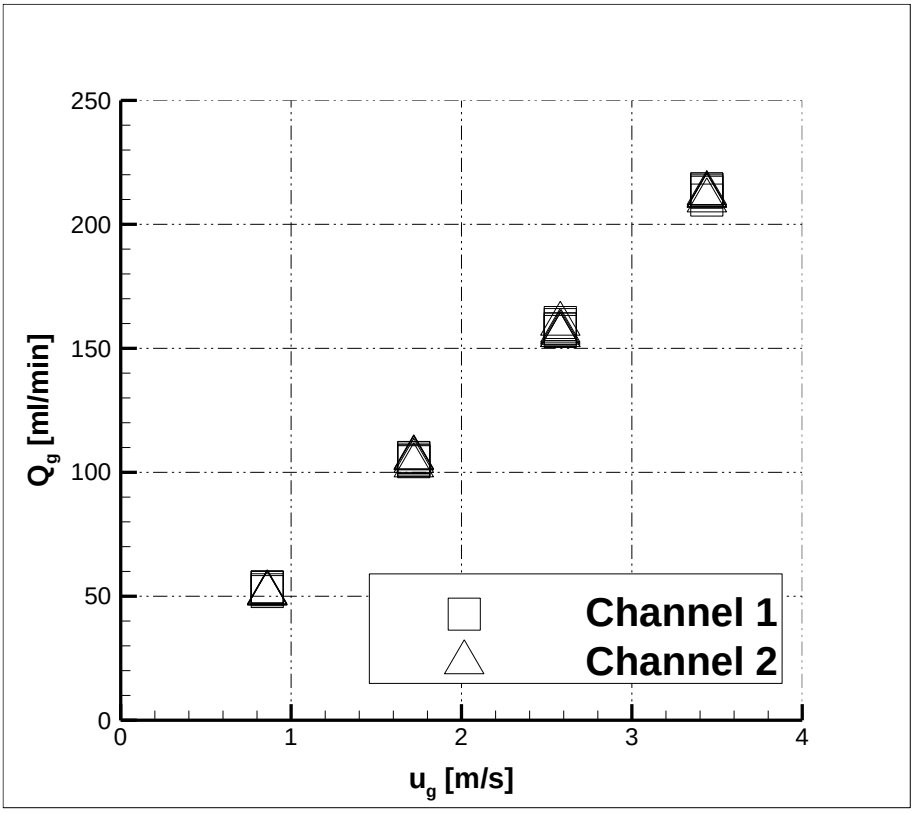

Figure 38: Measured gas flow rates of the two channels, respectively, under no liquid injection condition in Channel 2.

4.2.2 Two-phase Flow Patterns

In experiment, only film flow patterns were observed in the two-phase flow channel, i.e. Channel 2, under all the testing conditions, as shown in Fig. 39. From Fig. 39 (a), it is seen that liquid film is developed along the upper side of the channel and dragged towards the outlet by the air flow. As the superficial air velocity increases, the film thickness decreases, as indicated by Lewis and Wang [40] and theoretical estimate [58]. In Fig. 39 (b) and (c), the liquid film in the Channel 2 is very thin as revealed by the camera, i.e. liquid water is drained efficiently out of Channel 2 by air flow. It is also important to note that water tends to accumulate near the outlet of the Channel 2, which is observed by Adroher and Wang [21], Lewis et al. [62], and Wang et al. [2]. Z.Lu et al. [63] found that water tends to build up at the transition area from channel to exit header of parallel micro-channels of PEM fuel cells. Lewis and Wang [62] investigated the two-phase flow in a single micro-channel with outlet expanding to a large manifold, indicating that it can significantly increase the overall pressure drop. Wang et al. [2] indicated that channel heterogeneity may cause water accmulation.

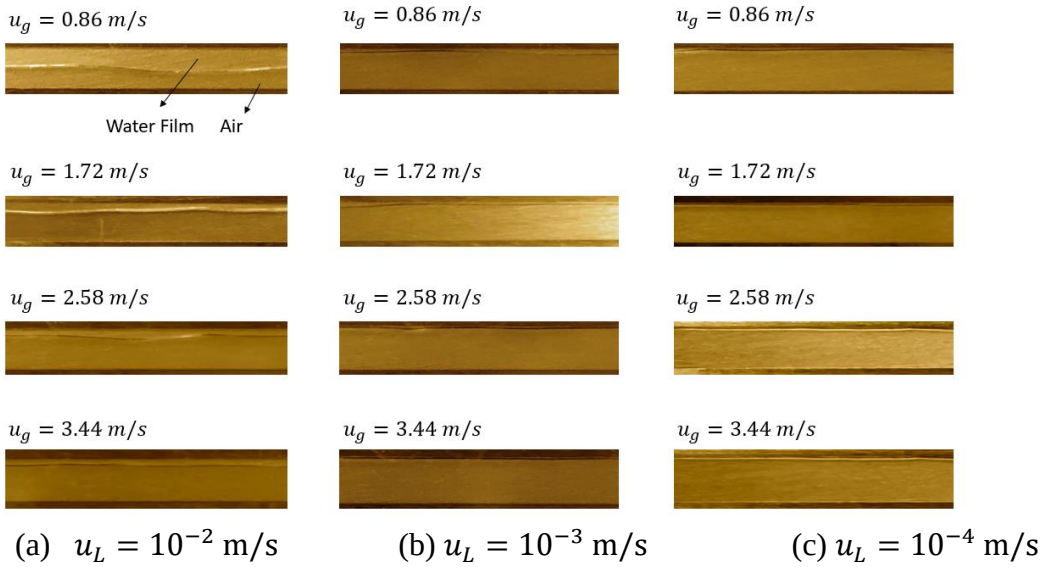

Figure 39: Two-phase flow patterns in Channel 2.

4.2.3 Flow Maldistribution and Gas Flow Rate Ratio

The volumetric gas flow rate in each channel was measured when reaching a steady-state pressure drop. Since Channel 1 only experiences single-phase flow and the pressure drops in the two channels are always the same at any time, the volumetric flow rate, Q_1, in Channel 1 is determined by:

$$Q_1 = u_{g_1} A \quad (4.4)$$

where u_{g_1} is superficial air velocity given by (4.1), in which ΔP is the experimentally measured pressure and A is the cross-section area. Then, the volumetric flow rate Q_2 in Channel 2 is given by:

$$Q_2 = Q_{total} - Q_1 \quad (4.5)$$

, where Q_{total} is the total flow rate injected into the inlet manifold. Note that Q_2 in Eq. (4.5) is obtained from pressure drop measurement, instead of direct measurement of the gas flow rate in Channel 2. The ratio of the air flow rates in the two channels $\frac{Q_2}{Q_1}$ is defined as a direct measure to flow maldistribution. A small ratio means severe flow maldistribution. A value approaching to unity means slight maldistribution. For two extreme cases, $\frac{Q_2}{Q_1} = 1$ corresponds to no maldistribution and $\frac{Q_2}{Q_1} = 0$ for complete blockage of Channel 2.

In addition, because of the identical cross-sectional areas in Channel 1 and 2,

$$\frac{Q_2}{Q_1} = \frac{u_{g_2}}{u_{g_1}} \quad (4.6)$$

where u_{g_2} is the superficial air velocity in Channel 2. Note that one will have average superficial gas velocity u_g,

$$u_{g_1} + u_{g_2} = 2u_g \quad (4.7)$$

In experiment, we measured Q_1 and Q_2 directly, thus the ratio can be calculated by these two measurements. Fig. 40-42 shows the $\frac{Q_2}{Q_1}$ ratio from direct flow rate measurement of Q_1 and Q_2 as a function of the average superficial gas velocity u_g at three different superficial liquid velocities in Channel 2. Fig. 40 shows that the flow rate ratio increases with the superficial air velocity at superficial water velocity $u_L = 10^{-2}$ m/s with the ratio reaching about 0.65 under the gas velocity of 3.44 m/s. This is because a large air velocity will improve liquid removal and thus reduce the liquid film thickness. When the air velocity decreases to 0.86 m/s, the ratio approaches 0.2, showing that the majority of the air flow takes the path of Channel 1 and consequently severe flow maldistribution occurs.

Similar trend is observed in the case for $u_L = 10^{-3}$ m/s under $u_g > 1.5$ m/s as shown in Fig. 41: The flow rate ratio reaches 0.71 at the gas velocity of 3.44 m/s. Around $u_g = 1.5$ m/s, there is a transition, where the trend of the $\frac{Q_2}{Q_1}$ ratio may go two pathways with one following the trend of $u_L = 10^{-2}$ m/s and the other reverse. This transition is possibly due to the exit behavior near the outlet: it is observed that water accumulates near the outlet, leaving a small passageway for air flow, and the passageway may widen as the average air flow velocity decreases to 0.86 m/s at this liquid water velocity. At $u_g = 0.86$ m/s, the flow rate ratios measured from repeating experiments show values of around 0.52 and 0.69, respectively, which is possibly due to the unstable flow at the channel outlet.

For $u_L = 10^{-4}$ m/s, as seen in Fig. 42, similar trend is again indicated for $u_g > 1.5$ m/s, and the ratio at the highest u_g is almost the same (about 0.7) as the case at $u_L = 10^{-3}$ m/s. This is possibly due to the fact that the two-phase dynamics at the outlet plays an important role in gas flow rate distribution. As shown in Fig. 44 which presents the two-phase images at the Channel 2

outlet: liquid accumulation is present and greatly narrows down the air flow passage. At the air velocity around 1.5 m/s, transition also appears in the $u_L = 10^{-4}$ m/s curve, which shows the trend of the gas rate ratio changes. The ratio even reaches 0.76 under u_g of 0.86 m/s. A number of independent repeating experiments were conducted under this u_L, as shown in Fig. 43, and confirmed the observation of the transition. Again, it may relate to transition of the outlet's two-phase dynamics, which shows the gas passage decreases to some degree as the air velocity increases towards 1.5 m/s, as shown in Fig. 44 (a) and (b) and continues to increase as air velocity grows away from 1.5 m/s, which is shown in Fig. 44 (b) and (c). The fundamental reason for this change is unclear, demanding further analysis on two-phase flow dynamics at the outlet. In addition, the flow rate ratio can be calculated using Eq. (4.4) and (4.5) from u_g in Channel 1 only instead of direct measurements of u_g in Channel 1 and Channel 2. Fig. 45 compares the flow rate ratio from the two methods. It shows that the data agrees very well under all the testing conditions. To determine how well the experimental data of flow rate ratio matches with the value given by equation (4.4) and (4.5), the mean absolute percent error $e_{\%}$ is defined as:

$$e_{\%} = \frac{1}{n}\sum_{i=1}^{n} |\Delta r_{\%}| \quad (4.8)$$

where $\Delta r_{\%}$ is defined as the difference between the flow rate ratios by the average of the two methods. $e_{\%}$ is less than 4% for all the data in this figure.

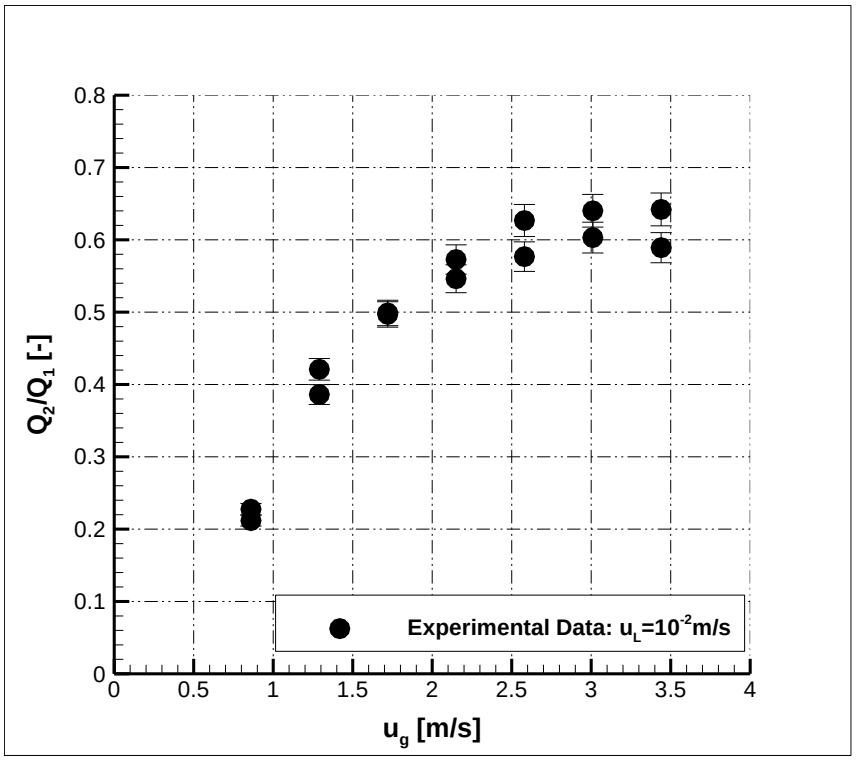

Figure 40 : Flow rate ratio vs the superficial gas velocity at $u_L = 10^{-2}$ m/s.

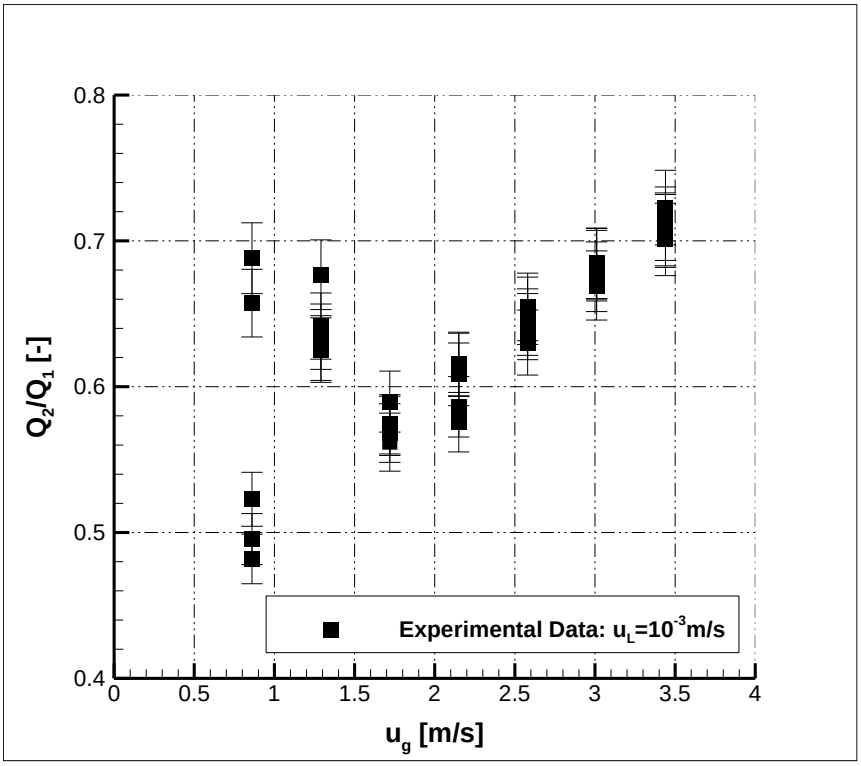

Figure 41: Flow rate ratio vs the superficial gas velocity at $u_L = 10^{-3}$ m/s.

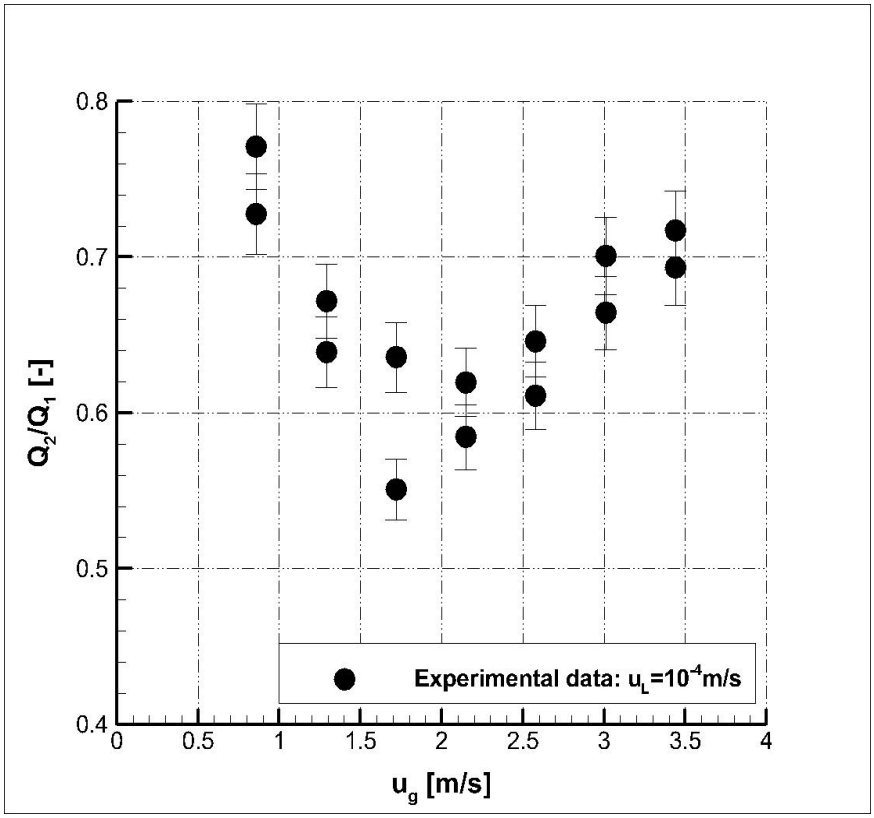

Figure 42: Flow rate ratio vs superficial gas velocity at $u_L = 10^{-4}$ m/s.

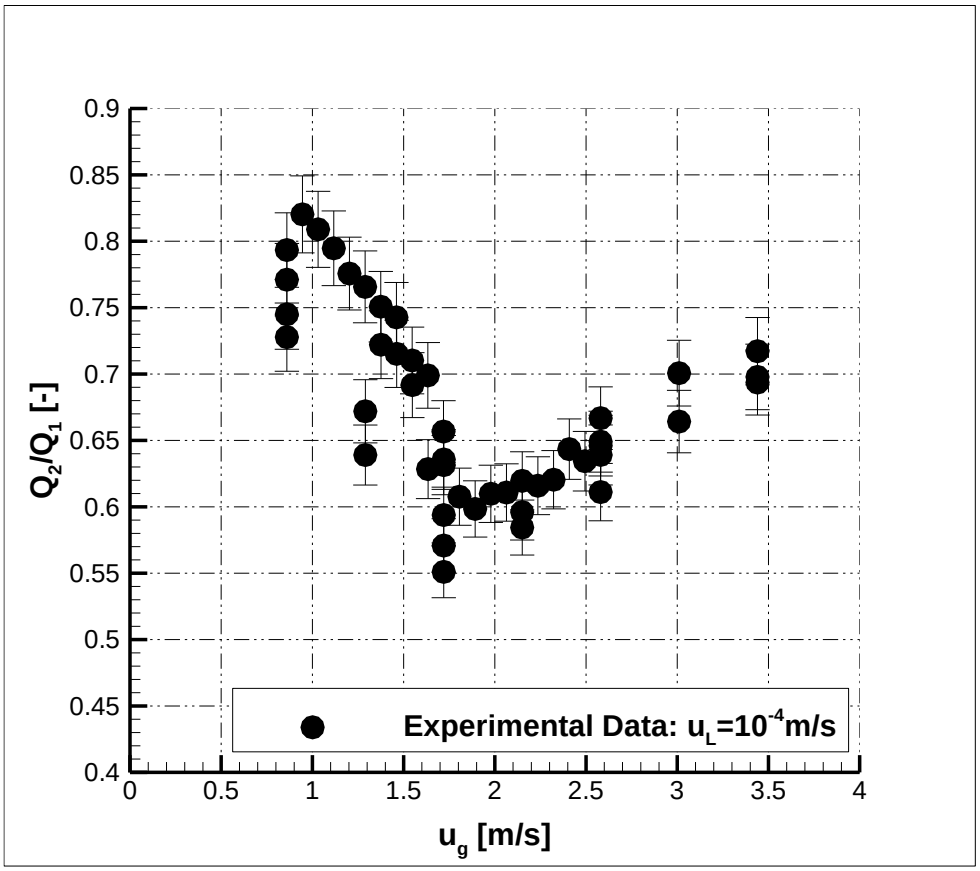

Figure 43: Repeating experiment of flow rate ratio study at $u_L = 10^{-4}$ m/s.

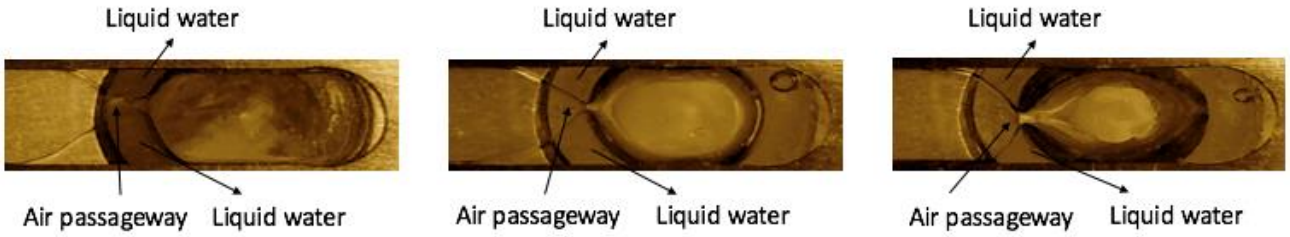

(a) $u_g = 0.86$ m/s (b) $u_g = 1.72$ m/s (c) $u_g = 3.44$ m/s

Figure 44: Exit behavior of Channel 2 at $u_L = 10^{-4}$ m/s.

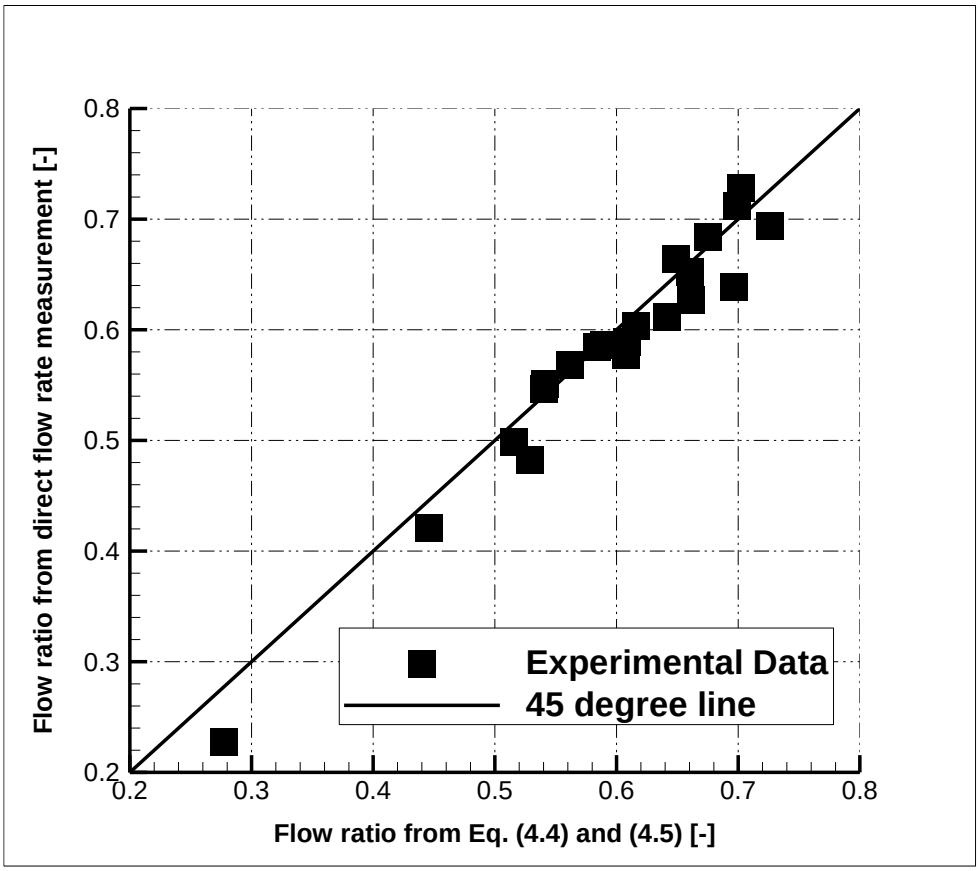

Figure 45: Gas flow rate ratio from direct flow rate measurement versus that from Eq. (4.4) and (4.5) using pressure measurement.

4.2.4 Pressure Drop

Fig. 46 and 47 shows the pressure drop history across the two channels for the entire period of the increasing u_g test under two superficial liquid velocities: $u_L = 10^{-3}$ m/s and $u_L = 10^{-4}$ m/s, respectively. Initially, the single phase flow ran at $u_g = 0.86$ m/s in both channels till steady state. Then, liquid water was injected to Channel 2 at a constant flow rate with a series of step changes in u_g. It can be seen that the pressure jumps as the air flow rate steps up. The seven steps, as shown in the two figures, correspond to the pressure history at seven different air flow rates, as shown in Table II. The pressure oscillates greatly at the initial period after u_g

changes, then becomes more stabilized, where the time average is around a constant value. Note that small oscillation still exists in the “steady state”, which is probably due to the dynamic two-phase flow near the channel outlet. However, the pressure oscillation is almost negligible when compared to the total pressure drop. The air flow rates were measured at “steady state”.

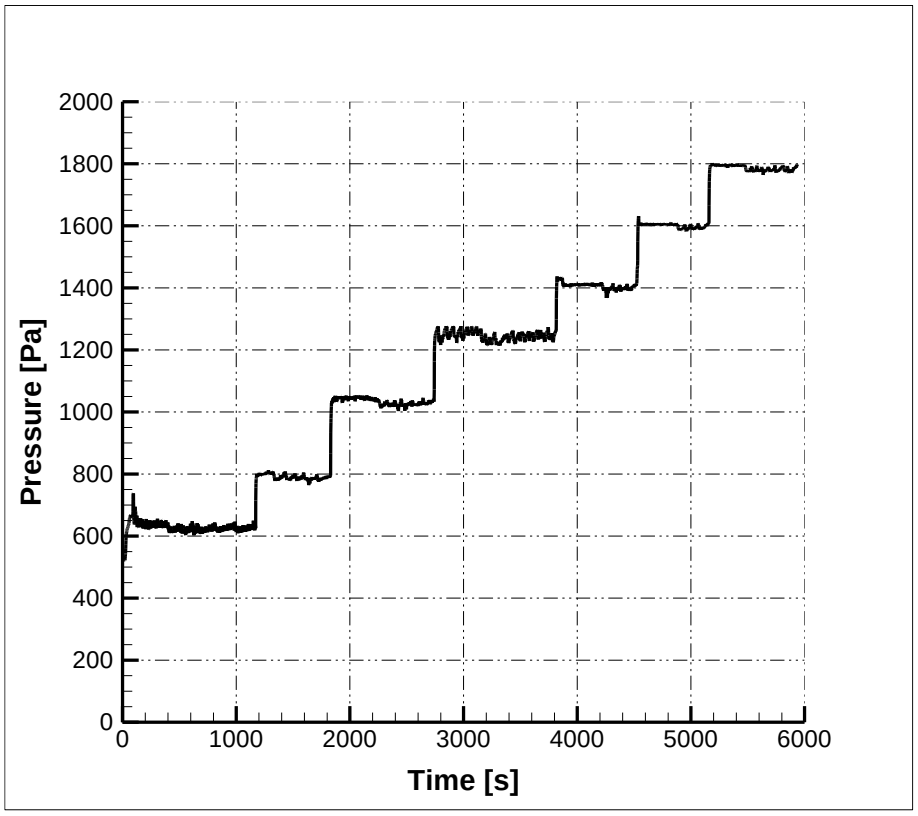

Figure 46: Pressure history vs time at $u_L = 10^{-3}$ m/s.

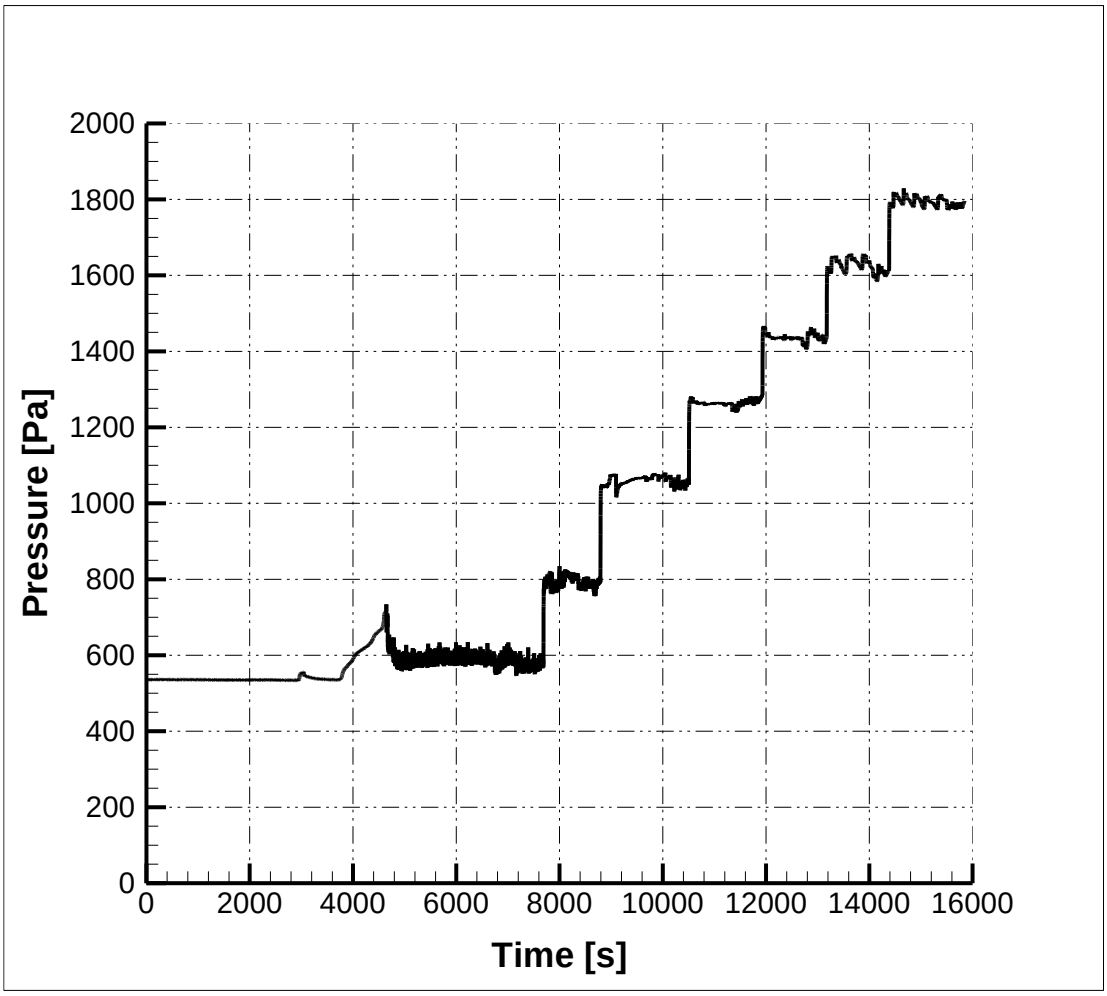

Figure 47: Pressure history vs time at $u_L = 10^{-4}$ m/s.

Fig. 48 shows the pressure drop in Channel 1 against the superficial air velocity from direct Q_1 measurement in comparison with the theoretical prediction, Eq. (4.1), indicative of a good match. Note that the pressure drop in experiment shows a dynamic behavior due to the impact from Channel 2, which falls in the two-phase flow regime. The time-average value of the pressure drop measurement data is used for comparison with the theoretical results. Fig. 49 presents the pressure drop in Channel 2 against the superficial air velocity from direct Q_2 measurement, in comparison with the experimental work for a single micro-channel by Lewis and Wang [40, 62]

and the single-phase flow pressure drop from Eq. (4.1). The experimental data lies above the theoretical line of the single-phase pressure due to the presence of liquid water in Channel 2, which narrows down the gas flow passage. In general, the larger liquid water injection rate, the more deviation from the theory line of the single-phase flow. This deviation is the primary driven force, leading to flow maldistribution. In general, two-phase pressure amplifier (ϕ) characterizes the pressure increase due to presence of the liquid phase, defined by:

$$\phi = P_{2phase}/P_{1phase} \quad (4.9)$$

In this study, ϕ is not directly calculated, but the flow ratio $\frac{Q_2}{Q_1}$. This ratio, as a direct measure of flow maldistribution, is related to the pressure amplifier, ϕ, as shown in the below derivation:

From Eq. (4.1), one can obtain:

$$\frac{P_{g,Ch1}}{P_{g,Ch2,1phase}} = \frac{u_{g_1}}{u_{g_2}} \quad (4.10)$$

Because Channel 2 is subject to two-phase flow, the real pressure drop is the two-phase pressure, $P_{g,Ch2,2phase}$, given by the ϕ definition:

$$P_{g,Ch2,2phase} = P_{g,Ch2,1phase}\phi \quad (4.11)$$

Because the real pressure drops in Channel 1 and 2 are always equal, one will reach:

$$\phi = \frac{Q_1}{Q_2} \quad (4.12)$$

From the above, the two-phase flow amplifier ϕ is directly related to flow maldistribution in this experimental setup. A large value of ϕ will lead to a small $\frac{Q_2}{Q_1}$, i.e. severe flow maldistribution. The above formula also shows that using the two-channel system in this experiment one can calculate the two-phase flow amplifier ϕ through direct measurement of the gas flow rates in both channels.

In addition, the two-phase pressure amplifiers reported in Lewis and Wang [62] are used to calculate the pressure drop, which are also plotted in the figure. Note that two amplifiers were obtained in Lewis and Wang [40,62], including one in the flow channel and the other for both flow channel and outlet expansion. To fit with this experiment which has a 2/3 length of channel subject to two-phase flow, the former amplifier obtained in Lewis and Wang [40] was applied to the 2/3 part of Channel 2. The outlet expansion's effect was accounted by the latter amplifier [62] subtracting the former one [40]. Again, it is seen that the measurement of the two-phase flow in Channel 2 agrees well with prediction of two-phase flow multipliers from two-phase flow experiment in a single channel.

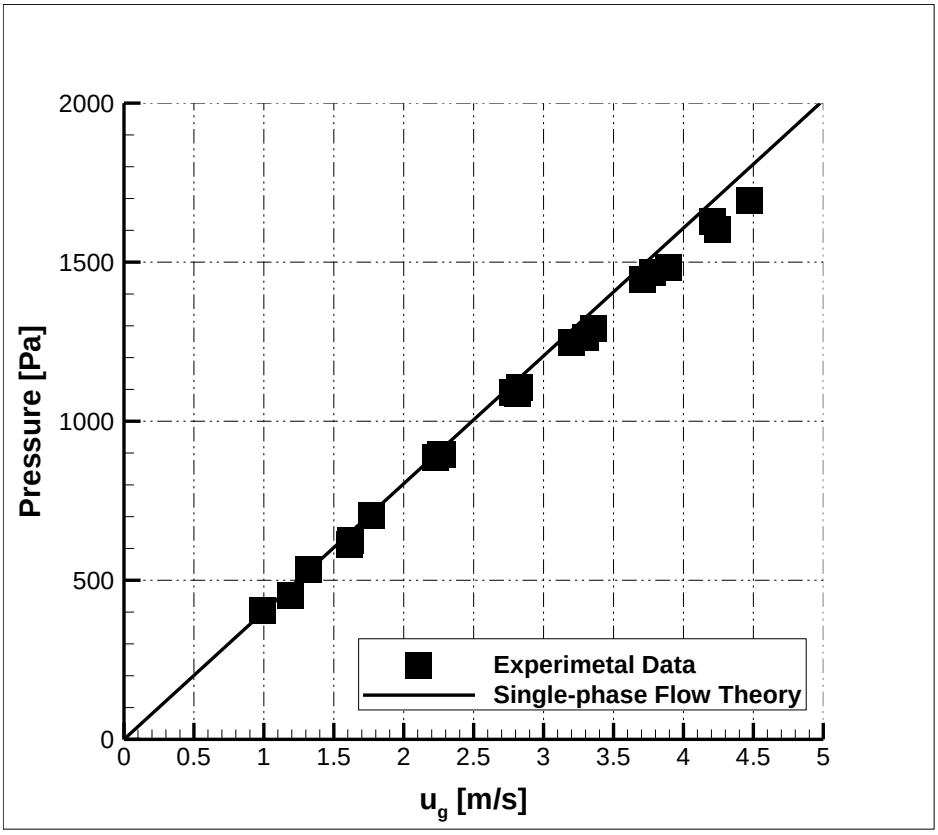

Figure 48: Gas pressure drop vs air velocity in Channel 1.

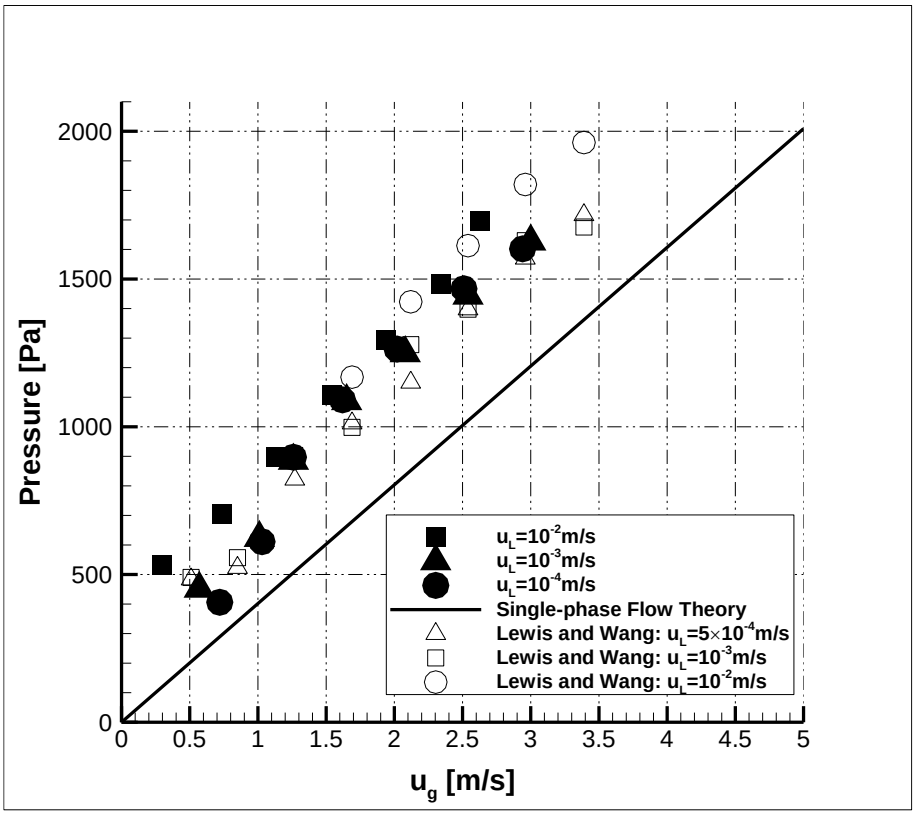

Figure 49: Gas pressure drop vs air velocity in Channel 2 in comparison with experimental work by Lewis and Wang [40,62] and theoretical single-phase pressure drop.

Chapter 5

Conclusions and Future Work

5.1 Conclusions

This study investigated two-phase flow in both single micro-channel and two micro-channel system. For the first, the VOF method was employed to investigate the two-phase flow dynamics in a thin gas flow channel with a dimension of $164 \times 3 \times 0.3$ mm. Various contact angles of the channel walls were studied to investigate their impacts on the two-phase interface where the air-liquid interaction occurs, film thickness, and pressure drop. The results were compared with various empirical models, two-fluid model, theoretical solutions and experimental results, in terms of the pressure drop, flow patterns and water volume fraction. We found that 1.) the wall contact angle impacts the two-phase interface in the thin channel by altering its curvature near the wall. The near-wall's two-phase interface shows an angle close to the wall's contact angle due to the dominant force of surface tension and wall impact. 2.) It was indicated that the contact angle may affect the optical observation of the liquid water thickness due to the interface curvature and raise uncertainty in the method of film thickness determination. 3.) The predicted flow remains in the stratified regime, as experimentally observed, for the contact angle ranging from 5° to 40°. The water fraction agreed well with the two-fluid model, analytical results, and experimental data. 4.) The predicted gas pressure agreed well with the experimental data, two-fluid model and some empirical models. The contact angle showed a negligible impact on the predicted pressure drop in the range of 5° to 40° including varying wall contact angles, in which the VOF predicted stable water film formation. For the contact angle over 40^{o}, the VOF

predicted unstable flows. The flow instability is under further investigation for future publication.

Two-phase flow dynamics in two-parallel micro-channels was investigated experimentally at the range of superficial air and water velocities similar to the VOF study to ensure the occurrence of film flow. Single-phase flow testing showed that the two channels are identical in dimension. The two channels were connected via the inlet manifold and the ambient outlet, with liquid water injected to Channel 2 only during the testing. Pressure drop and gas flow rates in each channel were experimentally measured, along with visualization of the two-phase flow. We found that:

1.) the film flow patterns were observed in Channel 2 for all the cases of study. It was also seen that the film flow pattern is thin under the two low liquid flow rates. In addition, two-phase flow in Channel 2 showed dynamic behaviors near the outlet: water tends to accumulate at the exit of Channel 2, which narrowed the air pathway.

2.) Gas volumetric flow rates were measured in each channel at various operating conditions. For $u_L = 10^{-2}$ m$/s$, the gas flow rate ratio increases monotonically with the superficial air velocity. As to $u_L = 10^{-3}\, m/s$, similar trend was only shown for $u_g > 1.5$ m/s, while two states were observed at $u_g = 0.86$ m/s, with one as low as 0.52 and the other as high as 0.69. As to $u_L = 10^{-4}\, m/s$, again similar trend was shown for $u_g > 1.5$ m/s, while for $u_g < 1.5$ m/s, the $\frac{Q_2}{Q_1}$ ratio increases as the total air rate decreases with a value as high as 0.76 at $u_g = 0.86$ m/s. This is likely related to the exit behaviors of two-phase flow in Channel 2.

3.) The pressure drop still oscillates when film flow pattern reaches steady-state. It is probably due to the water accumulation at the exit of Channel 2. This oscillation is negligible when compared to the total pressure drop across the channel. In addition, the averaged pressure

measurement at “steady state” of the two-phase flow in Channel 2 agrees well with prediction of two-phase flow multipliers from two-phase flow experiment in a single channel.

5.2 Recommendation for Future Research

5.2.1 VOF study of unstable flows

In the simulation study of two-phase flow in a single micro-channel, unstable flow patterns were observed for the contact angle greater than 40° under selected operational conditions. Flow patterns, time history of water fraction and pressure drop across the channel are of great interest to study. At this stage, it is unclear the observed unstable flows are due to the VOF numerical instability, selection of the time step, physical mechanisms, or droplet attachment (residual liquid) at the wall surface. The causes to instability under a contact angle over 40° need further investigation. In PEM fuel cells, droplets are formed randomly at the catalyst layer and further enters the gas channels via the GDL. Thus, it is also necessary to take into account of the porous micro-structure, as shown in Fig. 50, of the channel base in the future study [125].

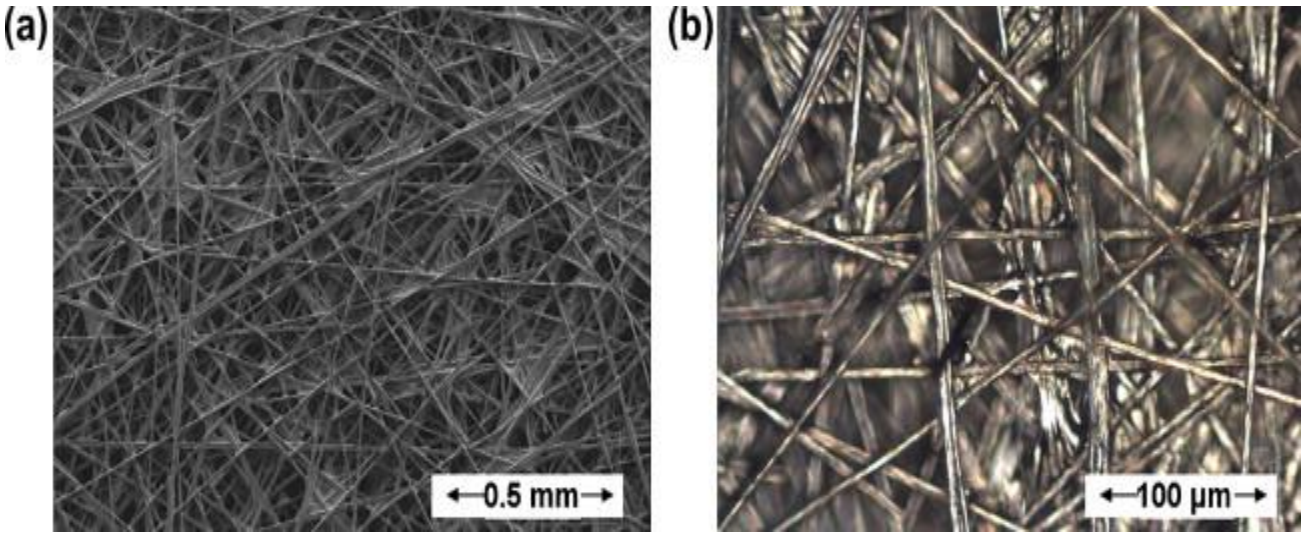

Figure 50: Microscope images of the carbon paper diffusion media used in PEFCs.

5.2.2 Exit Behaviors

For the air-water two-phase flow dynamics in micro-channels, water accumulation and dynamics at the channel-exit has been observed by other researchers [21, 62, 63], as shown in Fig. 51. It will partially block the exit of the channel and significantly affects the flow field by increasing the total pressure drop and decreasing the volumetric gas flow rate in the corresponding channel. The cause of exit behaviors, such as the surface tension, material heterogeneity, geometry, dimension of the micro-channel and operational conditions, requires further fundamental studies. The work is highly needed and important to understand two-phase flow dynamics, multichannel design, experimental design and control of two-phase flows in multiple gas flow channels.

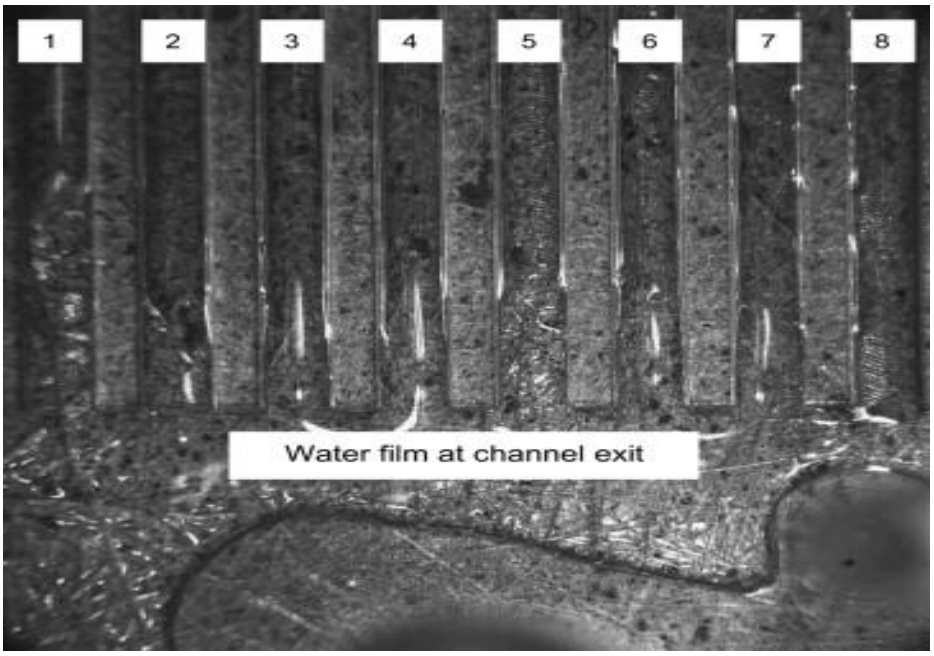

Figure 51: Water buildup at the channel-outlet manifold of PEM fuel cells [63].

References

[1] Y. Wang, K.S. Chen, J. Mishler, S.C. Cho & X.C. Adroher, A review of polymer electrolyte membrane fuel cells: technology, applications and needs on fundamental research, Applied energy, 88 (2011), pp. 981-1007.

[2] Y. Wang, S. Basu, C.Y. Wang, Modeling two-phase flow in PEM fuel cell channels, J. Power Sources, 179 (2008), pp. 603-617.

[3] J.G. Carton, V. Lawlor, A.G. Olabi, C. Hochenauer, G. Zauner, Water droplet accumulation and motion in PEM (Proton Exchange Membrane) fuel cell mini-channels, Energy, 39 (2012), pp. 63-73.

[4] A. Serizawa, Z.P. Feng, Z. Kawara, Two-phase flow in microchannels, Experimental Thermal and Fluid Science, 26 (2002), pp. 703-714.

[5] S.M. Ghiaasiaan, SI Abdel-Khalik, Two-phase flow in microchannels, Advances in heat transfer, 34 (2001), pp. 145-254.

[6] S.G. Kandlikar, Microscale and macroscale aspects of water management challenges in PEM fuel cells, Heat Transfer Engineering, 29 (2008), pp. 575-587.

[7] I.S. Hussaini, C.Y. Wang, Visualization and quantification of cathode channel flooding in PEM fuel cells, 187 (2009), pp. 44-451.

[8] K. Tüber, D. Pocza, C. Hebling, Visualization of water buildup in the cathode of a transparent PEM fuel cell, J. Power Sources, 124 (2003), pp. 403–414.

[9] S.D. Knights, K.M. Colbow, J. St-Pierre, D.P. Wilkinson, Aging mechanisms and lifetime of PEFC and DMFC, J. Power Sources, 127 (2004), pp. 127-134.

[10] J.P. Mayers, R.M. Darling, Model of carbon corrosion in PEM Fuel cells, J. Electrochem. Soc., 153 (2006), A1432–A1442.

[11] F. Barbir, H. Gorgun, X. Wang, Relationship between pressure drop and cell resistance as a diagnostic tool for PEM fuel cells, J. Power Sources, 141 (2005), pp. 96-101.

[12] P. Rodatz, F. Büchi, C. Onder, L. Guzzella, Operational aspects of a large PEFC stack under practical conditions, J. Power Sources, 128 (2004), pp. 208-217.

[13] P.C. Pei, M.G. Ouyang, W. Feng, L.G. Lu, H.Y. Huang, J.H. Zhang, Hydrogen pressure drop characteristics in a fuel cell stack, International Journal of Hydrogen Energy, 31 (2006), pp. 371-377.

[14] K.A. Triplett, S.M. Ghiaasiaan, Gas-liquid two-phase flow in microchannels Part I: two-phase flow patterns, International Journal of Multiphase Flow, 25 (1999), pp. 377-394.

[15] K.A. Triplett, S.M. Ghiaasiaan, Gas–liquid two-phase flow in microchannels: Part II: void fraction and pressure drop, International Journal of Multiphase Flow, 25 (1999), pp. 395-410.

[16] P.M.-Y. Chung, M. Kawaji, The effect of channel diameter on adiabatic two-phase flow characteristics in microchannels, International Journal of Multiphase Flow, 30 (2004), pp. 735-761.

[17] A. Serizawa, Z.P. Feng, Z. Kawara, Two-phase flow in microchannels, Experimental Thermal and Fluid Science, 26 (2002), pp.703-714.

[18] T. Cubaud, U. Ulmanella, C. Ho, Two-phase flow in microchannels with surface modifications, Fluid Dynamics Research, 38 (2006), pp.772-786.

[19] F.Y. Zhang, X.G. Yang, C.Y. Wang, Liquid water removal from a polymer electrolyte fuel cell, J. Electrochem. Soc., 153 (2006), pp. A225-A232.

[20] I.S. Hussaini, C.Y. Wang, Visualization and quantification of cathode channel flooding in PEM fuel cells, J. Power Sources, 187 (2009), pp. 444-451.

[21] X.C. Adroher, Y. Wang, Ex-situ and modeling study of two-phase flow in a single channel of polymer electrolyte membrane fuel cells, J. Power Sources, 196 (2011), pp. 9544-9551.

[22] W.H. McAdams, W.K. Woods, L.C. Heroman, Vaporization inside horizontal tubes II-benzene-oil mixtures, Trans. ASME, 64 (1942), pp. 193-200.

[23] A. Cicchitti, C. Lombardi, M. Silvestri, G. Soldaini, R. Zavalluilli, Two-phase cooling experiments pressure drop, heat transfer and burnout measurements, Energia Nucleare, 7 (1960), pp. 407-425.

[24] R.W. Lockhart, R.C. Martinelli, Proposed correlation of data for isothermal two phase flow, two component flow in pipes, Chem. Eng. Prog., 45 (1949), pp. 39-48.

[25] K. Mishima, T. Hibiki, Some characteristics of air-water two-phase flow in small diameter vertical tubes, Int. J. Multiphase Flow, 22 (1996), pp. 703-712.

[26] L. Sun, K. Mishima, Evaluation analysis of prediction methods for two-phase flow pressure drop in mini-channels, Int. J. Multiphase Flow, 35 (2009), pp. 47-54.

[27] W. Li, Z. Wu, A general correlation for adiabatic two-phase pressure drop in micro/mini-channels, Int. J. Heat Mass Transfer, 53 (2010), pp. 2732-2739.

[28] W. Zhang, T. Hibiki, K. Mishima, Correlations of two-phase frictional pressure drop and void fraction in mini-channel, Int. J. Heat Mass Transfer, 53 (2010), pp. 453-465.

[29] S.M. Kim, I. Mudawar, Universal approach to predicting two-phase frictional pressure drop for adiabatic and condensing mini/micro-channel flows, Int. J. Heat Mass Transfer, 55 (2012), pp. 3246-3261.

[30] Y. Wang, Porous-media flow fields for polymer electrolyte fuel cells II. Analysis of channel two-phase flow, Journal of the Electrochemical Society, 156 (2009), B1134-B1141.

[31] A. Nowamooz, G. Radilla, M. Fourar, Non-Darcian two-phase flow in a transparent replica of a rough-walled rock fracture, Water Resour. Res., 45 (2009), p. W07406.

[32] M. Fourar, R. Lenormand, A viscous coupling model for relative permeabilities in fractures, Paper SPE 49006, in: SPE Annual Technical Conference and Exhibition, New Orleans, LA, 1998.

[33] H. Huang, Z. Li, S. Liu, X.Y. Lu, Shan and chen type multiphase lattice boltzmann study of viscous coupling effects for two-phase flow in porous media, Int. J. Numer. Methods Fluids, 61 (2009), pp. 341-354.

[34] C.Y. Chen, R.N. Horne, M. Fourar, Experimental study of liquid-gas flow structure effects on relative permeabilities in a fracture, Water Resour. Res., 40 (2004), p. W08301.

[35] Z. Yu, O. Hemminger, L. Fan, Experiment and lattice Boltzmann simulation of two-phase gas–liquid flows in microchannels, Chemical Engineering Science, 62 (2007), pp. 7172-7183.

[36] A. Mehdizadeh, S.A. Sherif, W.E. Lear, Numerical simulation of thermofluid characteristics of two-phase slug flow in microchannels, International Journal of Heat and Mass Transfer, 54 (2011), pp. 3457-3465.

[37] D.Y. Qian, A. Lawal, Numerical study on gas and liquid slugs for Taylor flow in a T-junction microchannel, Chemical Engineering Science, 61 (2006), pp. 7609-7625.

[38] C. Fang, M. David, A. Rogacs, K. Goodson, Volume of fluid simulation of boiling two-phase flow in a vapor-venting microchannel, Frontiers in Heat and Mass Transfer (FHMT), 1 (2010), p. 013002.

[39] S. C. Cho and Y. Wang, Two-phase flow dynamics in a micro hydrophilic channel: A theoretical and experimental study, International Journal of Heat and Mass Transfer, 70 (2014), pp. 340-352.

[40] J.M. Lewis and Y. Wang, Two-phase frictional pressure drop and water film thickness in a thin hydrophilic microchannel, International Journal of Heat and Mass Transfer, 127 (2018), pp. 813-828.

[41] J.M. Lewis and Y. Wang, Two-phase frictional pressure drop in a thin mixed-wettability microchannel, International Journal of Heat and Mass Transfer, 128 (2019), pp. 649-667.

[42] S. C. Cho and Y. Wang, Two-phase flow dynamics in a micro channel with heterogeneous surfaces, International Journal of Heat and Mass Transfer, 71 (2014), pp. 349-360.

[43] Y. Wang, D.F.R. Diaz, K.S. Chen, Z. Wang, and X. C. Adroher, Materials, technological status, and fundamentals of PEM fuel cells–A review, Materials Today, 32 (2020), pp. 178-203.

[44] Y. Wang, & K.S. Chen, PEM fuel cells: thermal and water management fundamentals, Momentum Press, (2013)

[45] S. Maharudrayya, S. Jayanti and A.P. Deshpande, Pressure drop and flow distribution in multiple parallel-channel configurations used in proton-exchange membrane fuel cell stacks, Journal of Power Sources, 157 (2006), pp. 358-367.

[46] L.F. Zhang, W. Du, H.T. Bi, D.P. Wikinson, J. Stuper and H.J. Wang, Gas–liquid two-phase flow distributions in parallel channels for fuel cells, Journal of Power Sources, 189 (2009), pp. 1023-1031.

[47] L.F. Zhang, W. Du, H.T. Bi, D.P. Wikinson, J. Stuper and H.J. Wang, Gas–liquid two-phase flow patterns in parallel channels for fuel cells, Journal of Power Sources, 189 (2008), pp. 643-650.

[48] S.G. Kandlika, Z. Lu, W.E. Domigan, A.D. White, M.W. Benedict, Measurement of flow maldistribution in parallel channels and its application to ex-situ and in-situ experiments in PEMFC water management studies, International Journal of Heat and Mass Transfer, 52 (2009), pp. 1741-1752.

[49] Sadik Kakac, R.K. Shah and W. Aung, Handbook of single-phase convective heat transfer, 1987.

[50] R.K. Shah and A.L. London, Laminar flow forced convection heat transfer and flow friction in straight and curved ducts–A summary of analytical solutions, Standford University, Department of Mechanical Engineering, Tech. Rep., 11 1971.

[51] Y. Wang, S. Basu, C.Y. Wang, Modeling two-phase flow in PEM fuel cell channels, Journal Power Sources, 179 (2008), pp. 603-617.

[52] Y. Wang, C.Y. Wang, A non-isothermal, two-phase model for polymer electrolyte fuel cells, J. Electrochem. Soc., 153(2006), A1193.

[53] Y. Wang, C.Y. Wang, Two-phase transients of polymer electrolyte fuel cells, J. Electrochem. Soc., 154 (2007), B636.

[54] C.W Hirt, B.D Nichols, Volume of fluid (VOF) method for the dynamics of free boundaries, Journal of Computational Physics, 39 (1981), pp. 201-225.

[55] ANSYS FLUENT 12.0 Theory Guide.

[56] Z.Q. Niu, Y. Wang, K. Jiao and J.T. Wu, Two-phase flow dynamics in the gas diffusion layer of proton exchange membrane fuel cells: volume of fluid modeling and comparison with experiment, Journal of The Electrochemical Society, 165 (2018), pp. F613-F620.

[57] J.U. Brackbill, D.B. Kothe, C. Zemach, A continuum method for modeling surface tension, Journal of Computational Physics, 100 (1992), pp. 335-354.

[58] Steinbrenner, J. E. (2011), Two-phase flow phenomena in fuel cell microchannels, Stanford University.

[59] S.C. Cho, Y. Wang, and K.S. Chen, Droplet dynamics in a polymer electrolyte fuel cell gas flow channel: Forces, deformation, and detachment. I: Theoretical and numerical analyses, Journal of Power Sources, 206 (2012), pp. 119-128.

[60] A. Dukler, M. Wicks III, R. Cleveland, Fictional pressure drop in two-phase flow: B. An approach through similarity analysis, A.I.Ch.E J., 10 (1964), pp. 44-51.

[61] H.J. Lee, S.Y. Lee, Pressure drop correlations for two-phase flow within horizontal rectangular channels with small heights, Int. J. Multiph. Flow, 27 (2001), pp.783-796.

[62] J.M Lewis, Y. Wang, Investigating the pressure loss associated with two-phase flow in a rectangular microchannel suddenly expanding into a manifold, International Journal of Hydrogen Energy, 43 (2018), pp. 17444-17460.

[63] Z. Lu, S.G. Kandlikar, C. Rath, M. Grimm, W. Domingan, A.D. White, M. Hardbarger, I.P. Owejan, T.A. Tradbold, Water management studies in PEM fuel cells, Part II: Ex situ investigation of flow maldistribution, pressure drop and two-phase flow pattern in gas channels, International Journal of Hydrogen Energy, 34 (2009), pp. 3445-3456.

[64] Y.C. Zhao, G.W. Chen, Q. Yuan, Liquid-liquid two-phase flow patterns in a rectangular microchannel, American Institute of Chemical Engineers, 52 (2006), pp.4052-4060.

[65] S.C. Cho, Y. Wang, Two-phase flow dynamics in a micro hydrophilic channel: A theoretical and experimental study, 70 (2014), pp. 340-352.

[66] S.C. Cho and Y. Wang, Two-phase flow dynamics in micro channel with heterogeneous surfaces, International Journal of Heat and Mass Transfer, 71 (2014), pp. 349-360.

[67] P.C. Lee, F.G. Tseng, C. Pan, Bubble dynamics in microchannels. Part I: single microchannel, International Journal of Heat and Mass Transfer, 47 (2004), pp. 5575-5589.

[68] A. Salim, M. Fourar, J. Pironon, J. Sausse, Oil-water two-phase flow in microchannels: Flow patterns and pressure drop measurements, The Canadian Journal of Chemical Engineering, 86 (2008), pp. 978-988.

[69] T.T. Fu, L.J. Wei, C.Y. Zhu, Flow patterns of liquid-liquid two-phase flow in non-Newtonian fluids in rectangular microchannels, Chemical Engineering and Processing: Process Intensification, 91 (2015), pp. 114-120.

[70] T.A. Trabold, Minichannels in polymer electrolyte membrane fuel cells, Heat Transfer Eng., 26 (2005), pp. 3-12.

[71] M.B. Bowers and I. Mudawar, Two-phase electronic cooling using mini-channel and micro-channel heat sinks: Part 2 – flow rate and pressure drop constraints, Journal of Electronic Packaging, 116 (1994), pp. 298-305.

[72] Y. Peles, Two-phase boiling flow in microchannels-instabilities issues and flow regime mapping, Proceedings of ICMM2003-1069, pp. 559-566.

[73] P. Cheng and H.Y. Wu, Phase-change heat transfer in microsystems, International Heat Transfer Conference 13, 2006.

[74] T. S. Ravigururajan, Impact of channel geometry on two-phase flow heat transfer characteristics of refrigerants in microchannel heat exchangers, Journal of Heat Transfer, 120 (1998), pp. 485-491.

[75] K.K. Nielsen, K. Engelbrecht, D.V. Christensen, J.B. Jensen, A. Smith, C.R.H. Bahl, Degradation of the performance of microchannel heat exchanger due to flow maldistribution, Applied Thermal Engineering, 40 (2012), pp. 236-247.

[76] C. Anbumeenakshi and M.R. Thansekhar, Experimental investigation of header shape and inlet configuration on flow maldistribution in microchannel, Experimental Thermal and Fluid Science, 75 (2016), pp. 156-161.

[77] S. Baek, C. Lee, S. Jeong, Effect of flow maldistribution and axial conduction on compact microchannel heat exchanger, Cryogenics, 60 (2014), pp. 49-61.

[78] J. Wen, Y.Z. Li, A.M. Zhou, K. Zhang, J. Wang, PIV experimental investigation of entrance configuration on flow maldistribution in plate-fin heat exchanger, Cryogenics, 46 (2006), pp. 37-48.

[79] G. Kumaraguruparan, R. M. Kumaran, T. Sornakumar, T. Sundararajan, A numerical and experimental investigation of flow maldistribution in a micro-channel heat sink, International Communications in Heat and Mass Transfer, 38 (2011), pp. 1349-1353.

[80] S. Basu, C.Y. Wang, K. S. Chen, Two-phase flow maldistribution and mitigation in polymer electrolyte fuel cells, Journal of Electrochemical Energy Conversion and Storage, 6 (2009), pp. 031007 (1)-031007 (11).

[81] Z.Q. Niu, Z.M. Bao, J.T. Wu, Y. Wang and K. Jiao, Two-phase flow in the mixed-wettability gas diffusion layer of proton exchange membrane fuel cells, Applied Energy, 232 (2018), pp. 443-450.

[82] Z.Q. Niu, Y. Wang, K. Jiao and J.T. Wu, Two-phase flow dynamics in the gas diffusion layer of proton exchange membrane fuel cells: volume of fluid modeling and comparison with experiment, Journal of The Electrochemical Society, 165 (2018), F613-F620.

[83] Z.Q. Niu, J.T. Wu, Y. Wang and K. Jiao, Investigating the in-/through-plane effective diffusivities of dry and partially-saturated gas diffusion layers, Journal of The Electrochemical Society, 165 (2018), F986-F993.

[84] Z.Q. Niu, J.T. Wu, Z.M. Bao, Y. Wang, Y. Yin, K. Jiao, Two-phase flow and oxygen transport in the perforated gas diffusion layer of proton exchange membrane fuel cell, International Journal of Heat and Mass Transfer, 139 (2019), pp. 58-68.

[85] Z.Q. Niu, K. Jiao, Y. Wang, Q. Du, Y. Yin, Numerical simulation of two-phase cross flow in the gas diffusion layer microstructure of proton exchange membrane fuel cells, International Journal of Energy Research, 42 (2018), pp. 802-816.

[86] Z. Wang, C.Y. Wang, K. Chen, Two-phase flow and transport in the air cathode of proton exchange membrane fuel cells, J. Power Sources, 94 (2001), pp.40-50.

[87] L. You, H. Liu, A two-phase flow and transport model for the cathode of PEM fuel cells, Int. J. Heat Mass Transf., 45 (2002), pp. 2277-2287.

[88] S. Mazumder, J.V. Cole, Rigorous 3-D mathematical modeling of PEM fuel cells II. Model predictions with liquid water transport, J. Electrochem. Soc., 150 (2003), pp. A1510-A1517.

[89] U. Pasaogullari, C.Y. Wang, Two-phase modeling and flooding prediction of polymer electrolyte fuel cells, J. Electrochem. Soc., 152 (2005), pp. A380-A390.

[90] A.L. Dicks, & D.A. Rand, Fuel cell systems explained, John Wiley & Sons, (2018).

[91] G. He, P. Ming, Z. Zhao, A. Abudula, Y. Xiao, A two-fluid model for two-phase flow in PEMFCs,
J. Power Sources, 163 (2007), pp. 864-873.

[92] Q. Ye, T. Van Nguyen, Three-dimensional simulation of liquid water distribution in a PEMFC with experimentally measured capillary functions, J. Electrochem. Soc., 154 (2007), pp. B1242-B1251.

[93] T. Berning, A three-dimensional, two-fluid model of PEM fuel cell cathodes**,** ECS Trans., 16 (2008), pp. 23-34.

[94] V. Gurau, T.A. Zawodzinski, J.A. Mann, Two-phase transport in PEM fuel cell cathodes, J. Fuel Cell Sci. Technol., 5 (2008), p. 21009.

[95] R. O'hayre, S.W. Cha, W. Colella, & F.B. Prinz, Fuel cell fundamentals, John Wiley & Sons, (2016).

[96] B. Sundén, & M. Faghri, Transport phenomena in fuel cells (Vol. 19), WIT press, (2005).

[97] K. Jiao, B. Zhou, P. Quan, Liquid water transport in straight micro-parallel-channels with manifolds for PEM fuel cell cathode**,** J. Power Sources, 157 (2006), pp. 226-243.

[98] Y.H. Cai, J. Hu, H.P. Ma, B.L. Yi, H.M. Zhang, Effects of hydrophilic/hydrophobic properties on the water behavior in the micro-channels of a proton exchange membrane fuel cell, J. Power Sources, 161 (2006), pp. 843-848.

[99] G. Hoogers, Fuel cell technology handbook, CRC press, (2002).

[100] P. Quan, M.C. Lai, Numerical simulation of two-phase water behavior in the cathode of an interdigitated proton exchange membrane fuel cell, J. Fuel Cell Sci. Technol., 7 (2010), pp. 0110171-01101714.

[101] A. Theodorakakos, T. Ous, M. Gavaises, J. Nouri, N. Nikolopoulos, H. Yanagihara, Dynamics of water droplets detached from porous surfaces of relevance to PEM fuel cells, J. Colloid Interface Sci., 300 (2006), pp. 673-687.

[102] A. Bazylak, D. Sinton, N. Djilali, Dynamic water transport and droplet emergence in PEMFC gas diffusion layers, J. Power Sources, 176 (2008), pp. 240-246.

[103] C. Fang, C. Hidrovo, F. Wang, 3-D numerical simulation of contact angle hysteresis for microscale two phase flow, J. Eaton, K. Goodson, Int. J. Multiph. Flow., 34 (2008), pp. 690-705.

[104] A. Golpaygan, N. Ashgriz, Multiphase flow model to study channel flow dynamics of PEM fuel cells: deformation and detachment of water droplets, Int. J. Comput. Fluid D., 22 (2008), pp. 85-95.

[105] C. Y. Wang, Fundamental models for fuel cell engineering, Chemical reviews, 104 (2004), pp. 4727-4766.

[106] E. Shirani, S. Masoomi, Deformation of a droplet in a channel flow, J. Fuel Cell Sci. Technol., 5 (2008), p. 041008.

[107] K. Tüber, D. Pócza, & C. Hebling, Visualization of water buildup in the cathode of a transparent PEM fuel cell, Journal of Power Sources, 124 (2003), pp. 403-414.

[108] I. Manke, C. Hartnig, M. Grünerbel, W. Lehnert, N. Kardjilov, A. Haibel, & H. Riesemeier, Investigation of water evolution and transport in fuel cells with high resolution synchrotron x-ray radiography, Applied Physics Letters, 90 (2007), p. 174105.

[109] J. Mishler, Y. Wang, R. Mukundan, J. Spendelow, D.S. Hussey, D.L. Jacobson, & R.L. Borup, Probing the water content in polymer electrolyte fuel cells using neutron radiography, Electrochimica acta, 75 (2012), pp. 1-10.

[110] Y. Wang, & K. S. Chen, Effect of spatially-varying GDL properties and land compression on water distribution in PEM fuel cells, Journal of The Electrochemical Society, 158 (2011), pp. B1292-B1299.

[111] L. Chen, T. Cao, Z. Li, Y. He, W. Tao, Numerical investigation of liquid water distribution in the cathode side of proton exchange membrane fuel cell and its effects on cell performance, Int. J. Hydrog. Energy, 37 (2012), pp. 9155-9170.

[112] Y. Wang, & X. Feng, Analysis of the reaction rates in the cathode electrode of polymer electrolyte fuel cells II. dual-layer electrodes, Journal of The Electrochemical Society, 156 (2009), pp. B403-B409.

[113] Y. Ding, R. Anderson, L.F. Zhang, X.T. Bi, D.P. Wilkinson, Simulations of two-phase flow distribution in communicating parallel channels for a PEM fuel cell, International Journal of Multiphase Flow, 52 (2013), pp. 35-45.

[114] X. Feng, & Y. Wang, Multi-layer configuration for the cathode electrode of polymer electrolyte fuel cell, Electrochimica acta, 55 (2010), pp. 4579-4586.

[115] Y. Wang, & M. Gundevia, Measurement of thermal conductivity and heat pipe effect in hydrophilic and hydrophobic carbon papers, International Journal of Heat and Mass Transfer, 60 (2013), pp. 134-142.

[116] Y. Wang, & K. S. Chen, Elucidating two-phase transport in a polymer electrolyte fuel cell, Part 1: Characterizing flow regimes with a dimensionless group, Chemical engineering science, 66 (2011), pp. 3557-3567.

[117] E. Mancusi, E. Fontana, A.A. Ulson de Souza, S.M.A. Guelli Ulson de Souza, Numerical study of two-phase flow patterns in the TS CrossMark gas channel of PEM fuel cells with tapered flow field design, Int. J. Hydrog. Energy, 39 (2014), pp. 2261-2273.

[118] Y. Wang, & K. S. Chen, Advanced control of liquid water region in diffusion media of polymer electrolyte fuel cells through a dimensionless number, Journal of Power Sources, 315 (2016), pp. 224-235.

[119] Y. Wang, & K. S. Chen, Through-plane water distribution in a polymer electrolyte fuel cell: comparison of numerical prediction with neutron radiography data, Journal of The Electrochemical Society, 157 (2010), pp. B1878-B1886.

[120] S.C. Cho, Y. Wang, & K.S. Chen, Droplet dynamics in a polymer electrolyte fuel cell gas flow channel: Forces, Deformation and detachment. II: Comparisons of analytical solution with numerical and experimental results, Journal of Power Sources, 210 (2012), pp. 191-197.

[121] R. Anderson, L.F. Zhang, Y.L. Ding, M. Blanco, X.T. Bi, D.P. Wilkinson, A critical review of two-phase flow in gas flow channels of proton exchange membrane fuel cells, Journal of Power Sources, 195 (2010), pp. 4531-4553.

[122] H.Y. Kim, S. Jeon, M. Song, & K. Kim, Numerical simulations of water droplet dynamics in hydrogen fuel cell gas channel, Journal of Power Sources, 246 (2014), pp. 679-695.

[123] P. Polverino, A. Esposito, & C. Pianese, Experimental validation of a lumped model of single droplet deformation, oscillation and detachment on the GDL surface of a PEM fuel cell, International Journal of Hydrogen Energy, 38 (2013), pp. 8934-8953.

[124] J.T. Wu, Y. Li, & Y. Wang, Three-dimension simulation of two-phase flows in a thin gas flow channel of PEM fuel cell using a volume of fluid method, International Journal of Hydrogen Energy, (2019),10.1016/j.ijhydene.2019.09.149.

[125] Y. Wang, S.C. Cho, R. Thiedamnn, V. Schmidt, W. Lehnert, X.H. Feng, Stochastic modeling and direct simulation of the diffusion media for polymer electrolyte fuel cells, International Journal of Heat and Mass Transfer, 53 (2010), pp. 1128-1138.

[126] D. L. Youngs, Time-dependent multi-material flow with large fluid distortion, Numerical Methods For Fluid Dynamics, 1982, pp. 273–285.